**FACULTY
OF MATHEMATICS
AND PHYSICS**
Charles University

BACHELOR THESIS

Adéla Kolembusová

Microstructure stability and resulting mechanical properties of a low-alloyed Mg-Zn-Gd alloy prepared by rapid solidification

Department of Physics of Materials

Supervisor of the bachelor thesis: RNDr. Daria Drozdenko, Ph.D.

Study programme: Physics

Prague 2024

I declare that I carried out this bachelor thesis on my own, and only with the cited sources, literature and other professional sources. I understand that my work relates to the rights and obligations under the Act No. 121/2000 Sb., the Copyright Act, as amended, in particular the fact that the Charles University has the right to conclude a license agreement on the use of this work as a school work pursuant to Section 60 subsection 1 of the Copyright Act.

In .... date ....

Author's signature

Title: Microstructure stability and resulting mechanical properties of a low-alloyed Mg-Zn-Gd alloy prepared by rapid solidification

Author: Adéla Kolembusová

Department: Department of Physics of Materials

Supervisor: RNDr. Daria Drozdenko, Ph.D.

Abstract: In this work, the thermal stability of the microstructure and the resulting mechanical properties of the low-alloyed Mg-0.56Zn-1.5Gd (at.%) alloy prepared by the rapidly solidified ribbon consolidation technique were studied. Scanning and transmission microscopy were used to characterise the microstructure in the initial state and after annealing for 2 h at various temperatures between 300 and 500 °C. The initial microstructure consists of small recrystallised grains with an average size of 550 nm and large non-recrystallised grains. Moreover, the processing technique applied to the low-alloyed Mg alloy resulted in the formation of solute-enriched stacking faults (SFs), cluster-arranged layers, and cluster-arranged nano-plates, homogeneously distributed in the grain's interior. The microstructure of the alloy remains unchanged during heat treatment up to 350 °C, and with further increase in temperature, grain growth and redistribution of the solute-enriched SFs take place. The changes in the mechanical performance of the material, revealed by microhardness measurements and uniaxial tensile and deformation loading, were addressed with respect to the evolution of the microstructure. It was revealed that annealing up to 350 °C leads only to a minor decrease in the mechanical properties.

Keywords: magnesium alloys, rapid solidification, microstructure, mechanical properties, thermal treatment

Název práce: Mikrostrukturní stabilita a výsledné mechanické vlastnosti nízkolegované Mg-Zn-Gd slitiny připravené rychlou solidifikací

Autor: Adéla Kolembusová

Katedra: Katedra fyziky materiálů

Vedoucí bakalářské práce: RNDr. Daria Drozdenko, Ph.D.

Abstrakt: Tato práce byla zaměřena na odhalení teplotního rozsahu, při kterém nedochází ke změnám v mikrostruktuře a výsledných mechanických vlastnostech nízkolegované slitiny Mg-0,56Zn-1,5Gd (at.%) připravené metodou rychlé solidifikace. K charakterizaci mikrostruktury výchozího stavu a stavů žíhané slitiny při různých teplotách od 300 do 500 °C po dobu 2 h, byla použita skenovací a transmisní elektronová mikroskopie. Počáteční mikrostruktura se skládá z malých rekrystalizovaných zrn o průměrné velikosti 550 nm a velkých nerekrystalizovaných zrn. Zpracování nízkolegované hořčíkové slitiny během přípravy navíc vede k tvorbě vrstevných poruch obohacených legujícími prvky, klastrově uspořádaných vrstev a klastrově uspořádaných nanoplátků, které jsou uvnitř zrn rovnoměrně rozmístěné. Během tepelného zpracovávání do 350 °C se mikrostruktura slitiny se nemění. Při vyšších teplotách však dochází k růstu zrn a přeuspořádání vrstevnatých poruch. Vývoj mechanických vlastností s ohledem na vývoj mikrostruktury byl studován měřením mikrotvrdosti a deformačními zkouškami v tlaku a v tahu. Bylo zjištěno, že žíhání do 350 °C vede pouze k nepatrnému poklesu mechanických vlastností.

Klíčová slova: hořčíkové slitiny, rychlá solidifikace, mikrostruktura, mechanické vlastnosti, tepelné zpracovávání

Contents

Introduction

An important challenge for the transportation industry today is the reduction of fuel consumption in order to lower both emissions and operational costs. This can be achieved for instance by reducing the weight of vehicles.

During the last decades, magnesium (Mg) alloys have been attracting considerable interest for transportation and engineering applications due to their low density (~ 1.74 g/cm^3), reasonable strength, good formability, and accessibility. Mg is the eighth most abundant element on earth. Pure Mg is produced either from the reduction of magnesium chloride with silicon or through electrolysis of magnesium chloride melts from seawater. As the lightest structural material, Mg is 35% lighter than aluminum (2.7 g/m^3) and over four times lighter than steel (7.86 g/m^3). Consequently, it is desired to use Mg instead of heavier engineering metals.

Mg alloys find applications across various industries including automotive, aerospace, sports, and electronics. In the aerospace sector, they are widely used in aircraft components such as thrust reversers, jet engine fan frames, helicopter transmission castings, and seat frames [1]. Furthermore, Mg-based materials could be also beneficial for the biomedical industry, due to their good biocompatibility, biodegradability, nontoxicity, and Young's modulus, which is almost identical to that of a natural bone [2, 3]. Mg alloys therefore have potential for biomedical implants, such as screws, fixing plates, or cardiovascular stents.

However, pure Mg presents a relatively low yield strength and unstable corrosion behavior, which limits its use. These properties can be improved by adding various alloying elements and using different processing techniques. Recently, the newly developed Mg-Zn-Y alloys have attracted significant attention due to their enhanced mechanical properties compared to conventional Mg alloys at both room and elevated temperatures [4, 5, 6, 7], particularly achieving a yield strength of 600 MPa in tension at room temperature. Moreover, the application of a rapidly solidified ribbon consolidation (RSRC) processing technique on low-alloyed Mg-Zn-Y alloys leads to further improvement of corrosion [8] and mechanical properties [9].

This work is focused on revealing the temperature range where the microstructure and the resulting mechanical properties of a low-alloyed MgZnGd alloy prepared by the RSRC technique are maintained stable.

1 Theoretical background

1.1 Crystal structure and deformation mechanisms of Mg and its alloys

Pure Mg has a hexagonal close-packed (hcp) structure (see Figure 1.1), which is formed by alternating two hexagonal atomic layers: placing the atoms of layer B above the trigonal holes of layer A, resulting in a $ABAB$ stacking sequence. The hcp unit cell is characterised by 2 lattice parameters, the length a, and the height c. Derived from the geometric packing of identical hard spheres, the ideal ratio of the two parameters is $\frac{c}{a} = \sqrt{\frac{8}{3}} \approx 1.633$. However, in common metals, this ratio deviates from the ideal value, which influences their mechanical behavior, such as the priority in the activation of slip systems and the necessity of twinning.
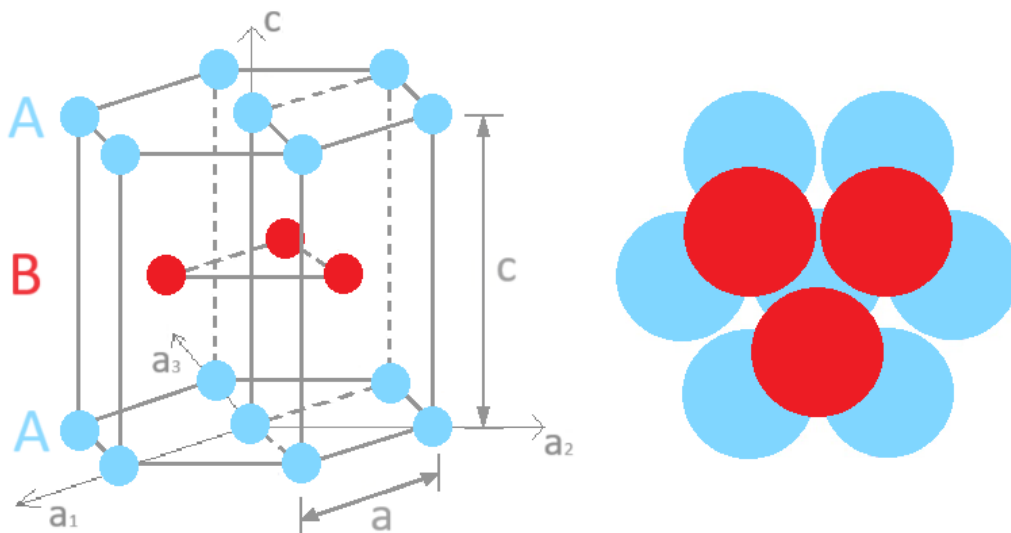

Figure 1.1 Hexagonal close-packed structure

The elementary plastic deformation mechanisms in hcp crystals are dislocation slip and twinning. A dislocation is a linear crystallographic defect. The direction and the magnitude of a dislocation is given by the Burgers vector. There are two types of dislocations as shown in Figure 1.2. An edge dislocation refers to the termination of a lattice plane in a crystal, distorting the surrounding planes of atoms, and is characterised by a Burgers vector perpendicular to the dislocation line. In a screw dislocation, the atoms are displaced on a helix around the dislocation line, which is parallel to the Burgers vector. However, most of the dislocations found in crystalline materials are not pure edge or pure screw, but rather a combination of both.

The movement of dislocations (dislocation slip) is one of the main mechanisms of plastic deformation. A slip system is defined by a slip plane, in which the dislocation propagates, and a slip direction. In a crystal structure, slip is activated in the plane with the densest atomic packing and in the direction where atoms are most closely packed. The minimum necessary stress to initiate slip is called
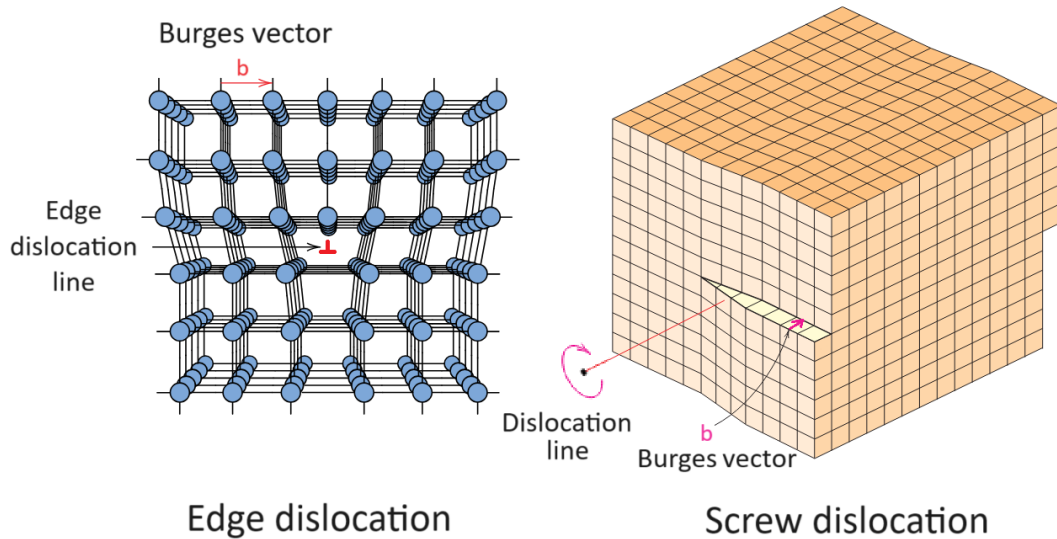
Figure 1.2   Edge and screw dislocations [10]

the critical resolved shear stress (CRSS). The resolved shear stress is the shear component of an applied tensile or compressive stress resolved along the slip plane. The resolved shear stress τ_{RSS} is related to the applied stress σ_{app} through the Schmid proportionality factor m [11] as

$$\tau_{RSS} = \sigma_{app}m = \sigma_{app}(\cos\phi\cos\lambda),$$

where ϕ is the angle between the normal of the slip plane and the direction of the applied force, and λ is the angle between the slip direction and the direction of the applied force, as shown in Figure 1.3. The Schmid factor is a geometric factor indicating how effectively the applied stress is resolved into shear stress on a slip system.
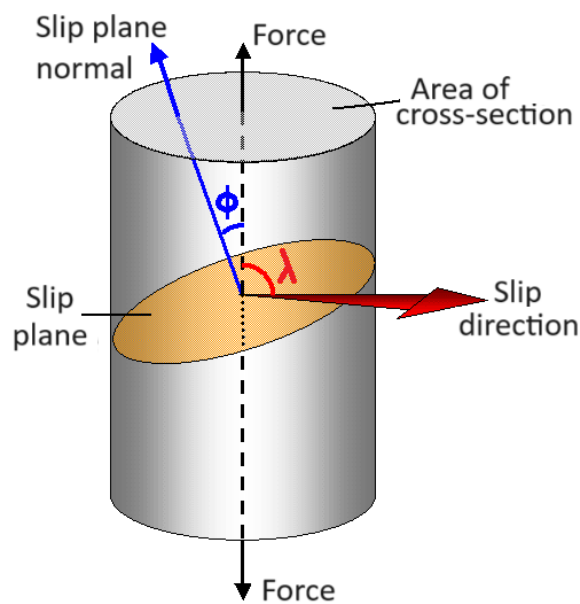
Figure 1.3   Visual representation of the resolved shear stress [12]

The hcp lattice structure limits the number of possible active slip systems. Dislocation slip can only occur on the basal $(0002)\langle a \rangle$, prismatic $\{1\bar{1}00\}\langle a \rangle$, pyramidal $\{1\bar{1}01\}\langle a \rangle$, and pyramidal $\{11\bar{2}2\}\langle c + a \rangle$ planes, as shown in Figure 1.4. When c/a $> \sqrt{8/3}$, the densest packing of atoms is in the basal planes, which promotes dislocation on the basal planes along the $\langle a \rangle$ direction, and when c/a $< \sqrt{8/3}$, the densest packing of atoms is in the prismatic plane [13].

Mg has a nearly perfect hcp structure with $c/a = 1.6236$ at 25 °C [14]. Thus, at room temperature, the primary slip occurs on the basal plane, along three $\langle a \rangle$ directions, constituting three slip systems, yet only two are independent. Mg polycrystals exhibit finite strains to failure, which according to the von Mises criterion for compatible (homogeneous) plastic deformation requires 5 independent slip systems to operate [15]. Other harder slips along the $\langle a \rangle$ direction exist on the prismatic and pyramidal planes, except they don't accommodate straining along the c-direction. For that, the slip on the pyramidal plane in the $\langle c + a \rangle$ direction needs to be activated. Its critical resolved shear stress (CRSS) is however very high at room temperature. Therefore deformation is accommodated by an additional deformation mechanism, mechanical twinning.

Twinning designates the process when a portion of a crystal is shearing a new position that mirrors the original crystal lattice. Among others, tensile twinning on the $\{10\bar{1}2\}$ planes and compression twinning on the $\{10\bar{1}1\}$ and $\{10\bar{1}3\}$ planes are the most commonly observed twinning systems in Mg alloys [16, 17].
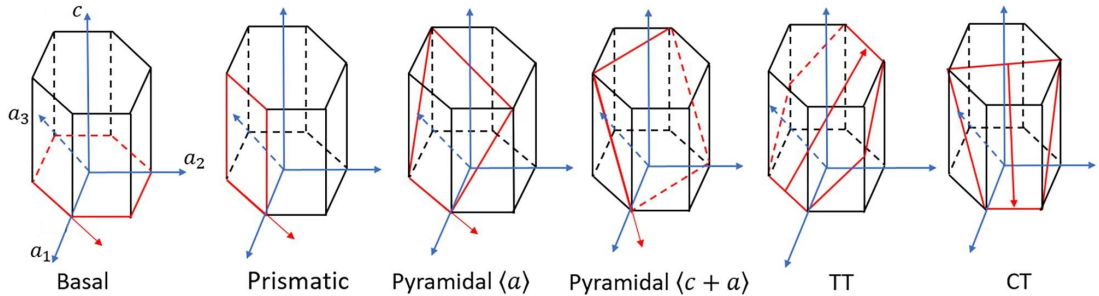
Figure 1.4 Slip and twinning systems in the hcp lattice [18], TT and CT stand for tensile and compressive twinning, respectively

The active deformation mechanisms are responsible for deformation behavior and thus, the final mechanical properties of a material. The relationship between the applied force per unit area and the elongation of the material per unit length is often represented by a stress-strain curve, usually obtained from tensile and compression tests. A generic deformation curve for metallic materials is shown in Figure 1.5. Under low stress, the material undergoes elastic deformation up to the yield point. In this case, the deformation is reversible, and the stress σ and strain ϵ are linked through Hooke's law as $\sigma = E\epsilon$, where E is the Young's modulus. Beyond the yield point, the material experiences plastic deformation, resulting in a permanent change in shape. When the transition between the elastic and plastic phases is gradual, the yield strength (YS) is defined as the stress causing 0.2 % plastic deformation. The material first undergoes strain hardening, where dislocation interactions increase its resistance to further deformation, until reaching the ultimate tensile/compressive strength, i.e., the maximum stress

the material can withstand. Beyond this point, the stress required for further deformation decreases due to the reduction of the cross-sectional area of the material (so-called necking), leading to subsequent fracture.
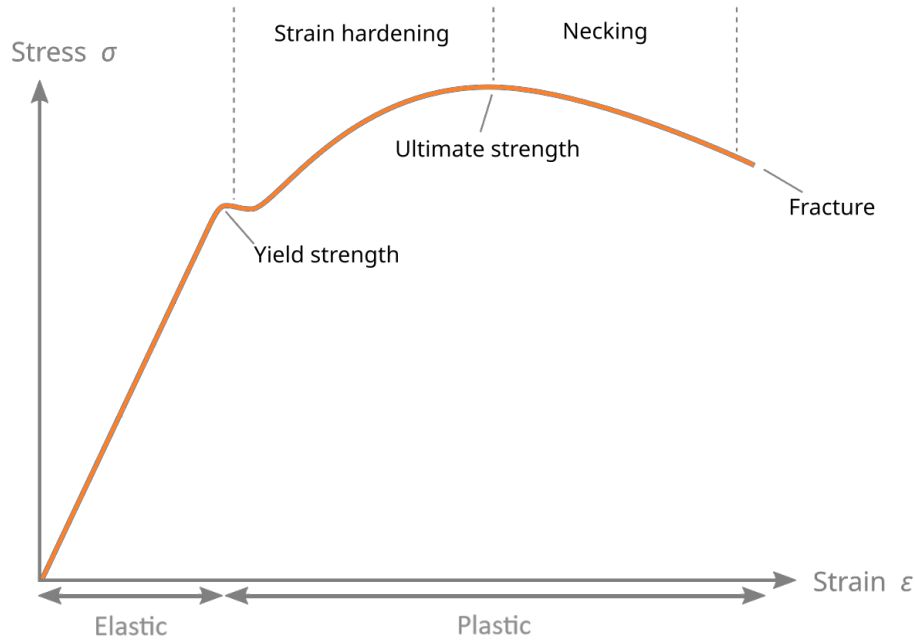
**Figure 1.5** Stress-strain curve of a metallic material

The deformation behavior of wrought Mg alloys is affected by hcp crystallographic lattice, grain size, and texture formed during processing [19]. Particularly, fine-grained materials are characterised by higher strength than coarse-grained materials because more grain boundaries can limit dislocation motion and grain size itself affects the activity of dislocation slip. The yield strength σ_y of a material, with respect to the average grain diameter d is given by the Hall-Petch equation as

$$\sigma_d = \sigma_0 + k_y d^{-1/2},$$

where σ_0 and k_y are constants specific to the particular material [20, 21]. However, the Hall-Petch equation does not work for bimodal microstructure (where few groups of grains with different sizes are present) or very small grains (where grain boundary sliding overcomes the dislocation slip mechanism). Moreover, a strong basal texture (with the c-axes of the hcp unit cells in the majority of grains oriented perpendicular to the extrusion axis) is commonly formed in extruded Mg alloys. Such texture together with the polar nature of tensile twinning (its preferential activation during compression perpendicular to the c-axis) leads to a significantly higher yield strength in tension than in compression, i.e., there is a tension-compression yield asymmetry [22, 23]. This effect can be minimised by suppressing twinning activity via the reduction of texture intensity and/or grain size [19, 24].

1.2 High-strength Mg alloys

Adding alloying elements can enhance the mechanical properties of Mg alloys. In particular, Mg alloys containing transition metals (TM) and rare earth (RE) elements, where a long-period stacking order (LPSO) phase is formed previously demonstrated outstanding mechanical properties compared to commercial Mg alloys [5]. The LPSO phase consists of "hard" layers enriched with the alloying elements, periodically separated by "soft" Mg layers. The periodicity of the stacking defines the type of the LPSO phase. The most observed LPSO types in MgZnY alloys are 10H, 18R, 14H, and 24R [25], represented in Figure 1.6.
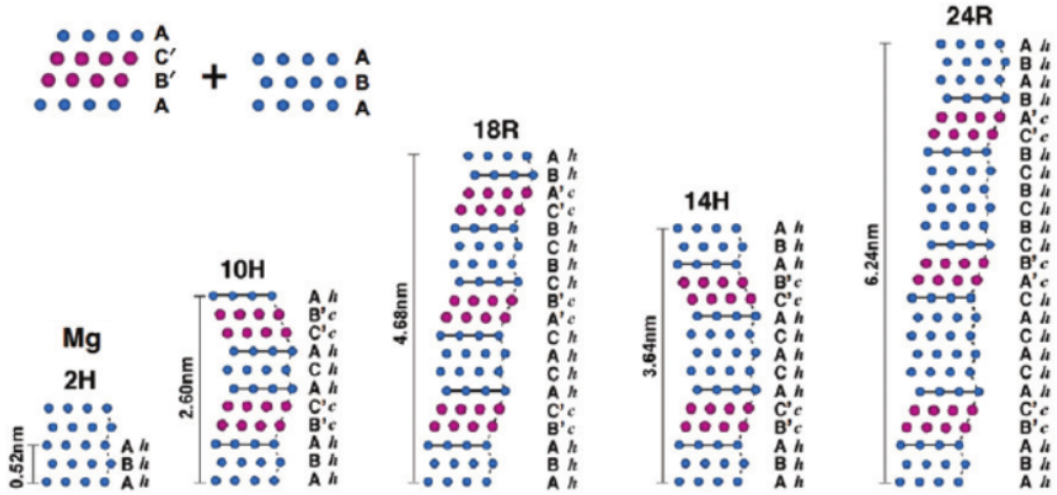
Figure 1.6 Classification of the LPSO phases [25]

As plastic deformation corresponds to the movement of large numbers of dislocations, the deformation capacity of an alloy depends on the ability of dislocations to move. Strengthening of a material can therefore be achieved by limiting the mobility of dislocations, for instance with grain boundaries or LPSO structures. The LPSO phase by its structure acts as an obstacle to dislocation motion, limits the activity of slip systems, and suppresses deformation twinning [26, 27]. Thus, the presence of precipitates or LPSO phase can reduce the tension-compression yield asymmetry, and in some cases, the asymmetry can even be reversed [28, 29, 30, 31]. The restriction of active deformation mechanisms leads to the activation of kinking (bending of the lattice) as an accommodating deformation mechanism [32]. Hence, the mechanical properties of the Mg-LPSO alloys are then affected by the volume fraction, orientation, and distribution of the LPSO phase, which depend on the amount of alloying elements and the methods of processing [29, 31, 33, 34, 35, 36, 37, 38]. Higher amounts of alloying elements tend to increase the strength since more LPSO phases can be formed. Moreover, it is reported, that the superior mechanical properties of extruded Mg-LPSO alloys are the result of the coexistence of fine dynamically recrystallised (DRX) α-Mg grains, which contribute to the ductility, and coarse non-DRX grains together with the LPSO phase, which enhance the strength [7].

Nevertheless, to achieve better biocompatibility, and from an economic point of view, it is desired to reduce the amount of the alloying elements. To do so, while maintaining the superior mechanical properties, modern processing techniques can be used, such as powder metallurgy or the ribbon consolidation technique. For instance, low-alloyed Mg-alloys prepared by the RSRC technique have shown superior strength, moderate elongation [9, 39] and high thermal stability of the microstructure [40].

It should be pointed out that in low-alloyed Mg-TM-RE alloys, the alloying elements aren't sufficiently abundant to form full LPSO phases. Instead, individual solute-rich stacking faults (SFs), cluster-arranged layers (CALs), and cluster-arranged nanoplates (CANaPs) are present. A stacking fault is a one-layer planar defect enriched with solute atoms and CALs are two-layer interruptions in the stacking sequence. The LPSO phase can thus be considered as an arrangement of CALs with a long periodicity. When the stacking arrangement is not periodic, more specifically the CALs are separated by 1 to 4 atomic layers of Mg, the structure is designated as CANaPs [41, 26]. For comparison, the structures are illustrated in Figure 1.7. The presence of solute-enriched SFs, CALs, and CANaPs, much like the LPSO phase, represent obstacles for dislocation motion, thereby contributes to the strengthening of the material [27].

Figure 1.7 Illustration of α-Mg lattice structure with SFs, CALs, LPSO, and CANaPs, where lines represent basal planes of the hcp structure

1.3 Electron microscopy

Detailed investigations of the microstructure with high resolution can be performed using scanning and transmission electron microscopy (SEM and TEM, respectively).

The scanning electron microscope uses a beam of electrons to scan a sample and form a magnified, high-resolution image of its surface. The primary electron beam used for imaging is generated by an electron gun. In thermal emission guns, the electrons are extracted from a tungsten filament by heating, whereas field guns use an electromagnetic field. The electrons are then accelerated by an accelerating voltage (usually 0.2 - 40 keV [42]) between the source and a positively charged anode plate, before entering the column. In the column, the beam is focused by electromagnetic lenses, and bent by scanning coils in the x and y

directions, allowing the focused beam to scan across the surface of the sample. To reduce electron scattering due to collisions with other molecules, the microscope operates under a high vacuum (below 10^{-4} Torr). A schema of a scanning electron microscope is shown in Figure 1.8.
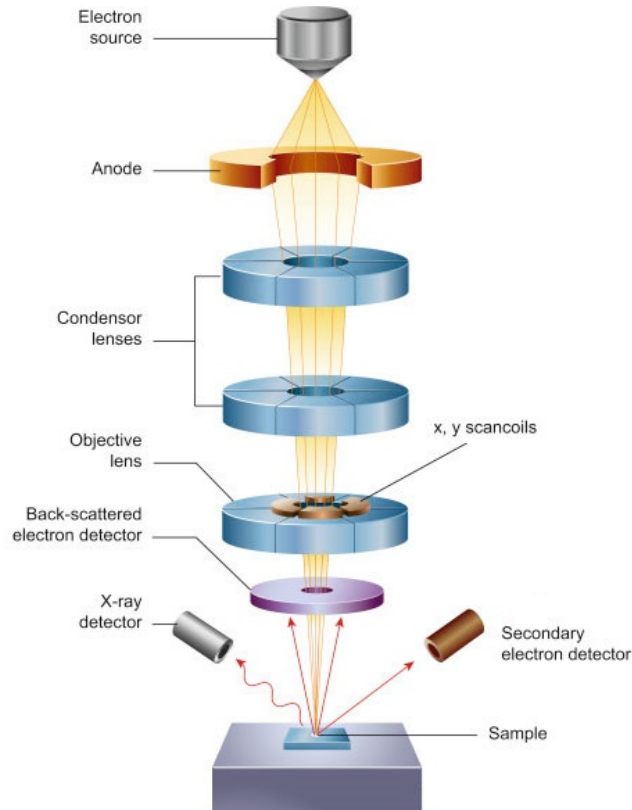
**Figure 1.8**   Scanning electron microscope [43]

When the electron beam hits the surface of the sample, the electrons interact with atoms in the sample. The interaction volume will depend on the energy of the primary electrons and the atomic number of the atoms in the sample material. As a result of the interaction, a variety of signals are produced. Most frequently the following signals are detected:

- Secondary electrons (SE): Low energy electrons emitted from inelastic scattering close to the surface. SE provide topographical information about the surface of sample.

- Back-scattered electrons (BSE): High energy electrons resulting from the elastic scattering of the primary electrons on the atoms of the material. BSE provide information about the composition of the sample. Heavier elements scatter more electrons and consequently appear brighter in the resulting image. Thus, this mode is particularly beneficial for revealing microstructure features in Mg-Zn-Y/Gd alloys, such as SFs, CALs, CANaPs enriched with solute elements (Zn,Y,Gd).

- Characteristic X-rays: Emitted when an ionised atom returns to its ground state, allowing the identification of the elements present in the sample.

Information about the crystallographic nature of a sample, particularly the grain structure, grain orientation, and phase can be obtained using the electron backscatter diffraction (EBSD) technique. For EBSD mapping, the sample is tilted in the scanning electron microscope at a high angle from the horizontal plane, usually 70°. This configuration maximises the intensity of the diffraction pattern, which is formed on a fluorescent phosphor screen. When electrons are incident on the crystal planes of a sample at an angle θ that satisfies the Bragg condition

$$n\lambda = 2d\sin\theta,$$

where n is an integer, λ is the wavelength of the electrons, and d is the spacing of the lattice planes, they are diffracted into a pair of cones, forming Kikuchi bands, Figure 1.9. The superposition of the Kikuchi bands resulting from the diffraction on lattice planes of various orientations creates the diffraction pattern. The diffraction patterns are then used to generate EBSD maps which display the phase, morphology, orientations, and boundaries of grains.
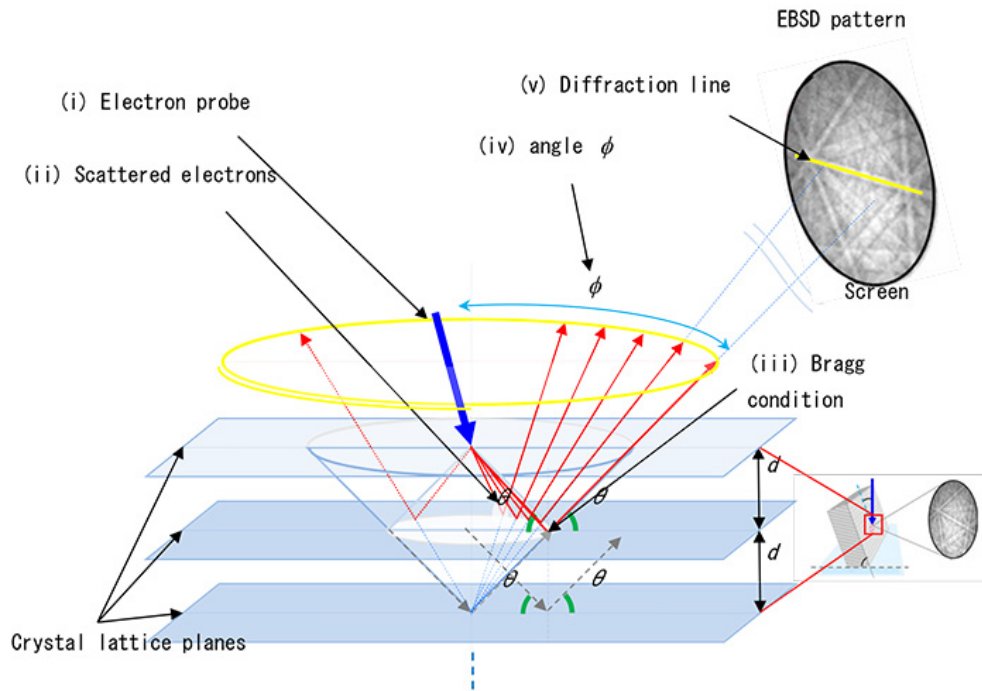
Figure 1.9   Illustration of the EBSD pattern formation [44]

The transmission electron microscopy (TEM) allows revealing microstructure down to atomic resolution, using the transmission of an electron beam through the studied sample. The transmission electron microscope can operate in the imaging or the diffraction mode, which are shown in Figure 1.10. In an electron gun, a thermal or field emission source emits electrons, which are accelerated by an accelerating voltage (usually 80 - 300 kV [45]) between the source and a positively charged anode plate. The electrons then enter a column of the microscope, where they are focused by electromagnetic lenses and apertures onto the sample. An objective lens under the sample is used to form the image or diffraction pattern (depending on the focus of the objective lens) from the transmitted electrons. This image or diffraction pattern is further magnified using intermediate and projector

lenses onto a viewing screen. Similarly to the scanning electron microscope, the transmission electron microscope requires a high vacuum to operate. The transmission electron microscope can also function in a scanning transmission electron microscopy (STEM) mode when equipped with scanning coils capable of focusing the electron beam into a fine spot and scanning across the sample surface.

The transmission electron microscope can function in following modes:

- Bright field (BF) imaging: Unscattered electrons are used to form the BF image. Areas of the sample that are thicker or denser appear darker on the resulting image because they scatter or absorb more electrons.

- Dark field (DF) imaging: Scattered electrons are used to form the DF image. Areas that scatter more appear brighter in the resulting image. DF is sensitive to crystallographic structure and orientation of the sample.

- Diffraction mode: Electrons that pass through the sample and are diffracted by the crystal lattice create a diffraction pattern. The diffraction pattern provides information about the crystallographic structure of the sample.

- Energy-Dispersive X-ray Spectroscopy (EDX): Emitted characteristic X-rays allow the identification of the elements present in the sample.
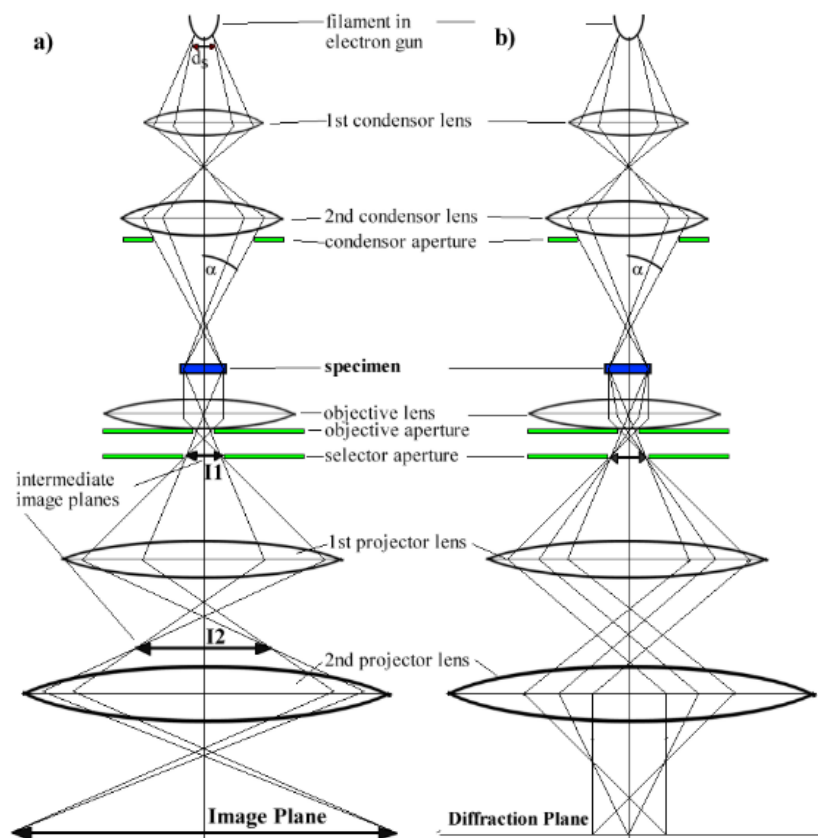
Figure 1.10 Transmission electron microscope operating in (a) imaging mode and (b) diffraction mode [46]

2 Aim of the thesis

The main aim of this work is to reveal the temperature range to maintain a stable microstructure and enhanced mechanical properties of the low-alloyed Mg-0.56Zn-1.5Gd (at.%) alloy prepared by the RSRC technique. A comprehensive characterisation of the microstructure development concerning the applied heat treatment is performed using scanning and transmission electron microscopy. The acquired knowledge is to be used for the description of the deformation mechanisms and thereby the mechanical performance of the investigated material. To achieve the main goal, the following particular tasks have to be completed:

- Characterisation of the microstructure and texture of the RSRC MgZnGd alloy in the initial state.

- Investigation of the microstructure development (including grain size, distribution of solute-enriched SFs, CALs, CANaPs) with respect to annealing for 2h at a temperature range from 350 °C up to 500 °C.

- Revealing the mechanical properties of the investigated alloy concerning the microstructure features introduced by the processing technique and the applied post-processing heat treatment.

3 Experimental procedure

3.1 Investigated material

For the present work, the Mg-0.56Zn-1.5Gd (at.%) alloy (hereafter, the MgZnGd alloy) was produced by gravity casting in an argon atmosphere. A schematic diagram of the preparation process is shown in Figure 3.1. The rapidly solidified (RS) ribbons were prepared by a single roller liquid quenching melt-spinning method at a roll peripheral speed of 42 m/s and cooling rate of $1.4 \cdot 10^5$ K/s. Then, the RS ribbons were consolidated by pressing into a copper billet with a diameter of 29 mm, degassing at 250 °C for 15 min, and by performing a direct vertical extrusion to a round bar of 10 mm in diameter at 350 °C, and an extrusion rate of 5.0 mm/s.

To investigate the thermal stability of the microstructure and mechanical properties, the samples of the RSRC MgZnGd alloy were subjected to annealing at 300 °C, 350 °C, 400 °C, 450 °C or 500 °C for 2 h, followed by water quenching.
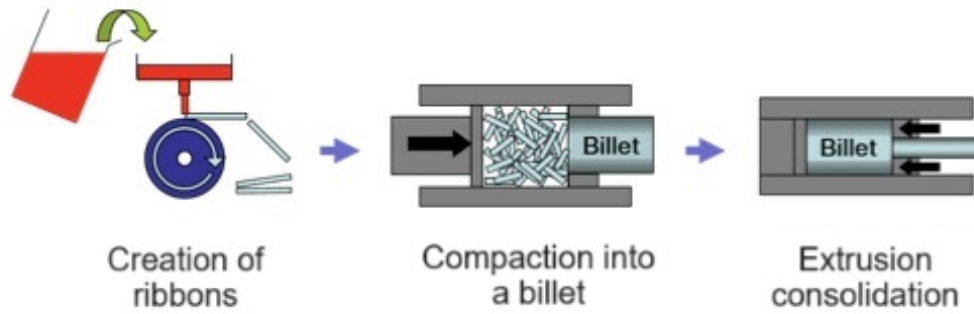
Figure 3.1 Preparation process of the RSRC material [47]

3.2 Experimental methods

Scanning electron microscopy

The investigation of the microstructure in the initial state and with respect to applied annealing was carried out using the Zeiss CrossBeam Auriga scanning electron microscope with an EDAX Velocity camera. The EBSD maps were collected with a step of 40 nm and an acceleration voltage of 15 kV. The EBSD maps were analysed using the TSL OIM software.

For SEM observations, samples were cut from the extruded bar of the MgZnGd alloy using the cut-off machine Accutom-50 from Struers perpendicular to the extrusion direction (ED). Samples of the material in the initial state and after annealing at respective temperatures were grinded on Struers SiC abrasive paper down to grit P4000, and then mechanically polished using diamond pastes down to 1 μm particle size. Subsequently, the samples were ion-beam polished using a Leica EM RE102 system.

Transmission electron microscopy

In order to reveal microstructure features in detail, the TEM observations have been performed using the JEOL 220FS HR transmission electron microscope. For TEM investigations, samples were cut from the extruded bar of the MgZnGd alloy perpendicular to ED using the cut-off machine Accutom-50 from Struers. Samples in the initial state and after annealing at respective temperatures were thinned to approximately 120 microns using SiC abrasive paper. From the thinned samples, smaller samples of diameter 2.7 mm were cut out using a punching machine. Subsequently, about 80 microns were removed using a dimple grinder and finally, the samples were ion-beam polished until the formation of a 1%-large hole using a Leica EM RE102 system.

Microhardness measurements

The Vickers microhardness measurements were carried out on a Qness Q10 with the Vickers EN ISO 6507 indentor with a test load of 0.1 kgf for an indentation time of 10 s (HV 0.1/10). The microhardness value was determined as the applied test force F divided by the surface area of the indent A as

$$HV = \frac{F}{A} = F \cdot \frac{2 \sin 136 \deg /2}{d^2},$$

where d is the average length between the two diagonals of the indentation.
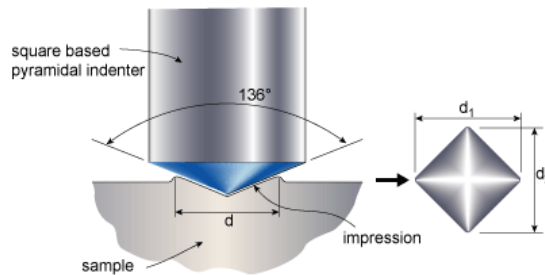
Figure 3.2 Vickers method to measure microhardness [48]

The sample's surface preparation for the microhardness measurements included grinding on SiC abrasive paper down to grit P4000, and then mechanical polishing using diamond pastes down to 1 μm particle size.

Deformation tests

In order to reveal the mechanical properties of the investigated material in the initial state and with respect to heat treatment, deformation tests in tension and compression were performed using the INSTRON 5882 universal testing machine. The material samples were subjected to uniaxial loading along ED at room temperature and a constant initial strain rate of $5 \cdot 10^{-4}$ s^{-1}.

The cylindrical samples with a height of 10 mm and a diameter of 7 mm were used for compression tests. For the tensile tests, the flat dog-bone samples with a gauge length of 10 mm, height of 2 mm, and thickness of 1 mm were used. To obtain data for the investigated alloy with respect to annealing conditions, the samples were annealed at 350 °C, 400 °C, and 500 °C for 2 h, followed by water quenching.

4 Results

4.1 Characterization of the initial microstructure

The inital microstructure of the investigated RSRC MgZnGd alloy is shown in Figure 4.1. A bimodal microstructure, consisting of small dynamically recrystallised (DRX), and large non-DRX α-Mg grains, is observed. The average grain size of the DRX grains is about 550 nm. The orientation map obtained by the EBSD technique was indexed for the α-Mg phase with a confidence index (CI) > 0.1. The corresponding texture, plotted in the form of the inverse pole figure, is characterised by a pronounced intensity at the $\langle 10\bar{1}0 \rangle$-pole given by the preferential orientation of non-DRX grains.
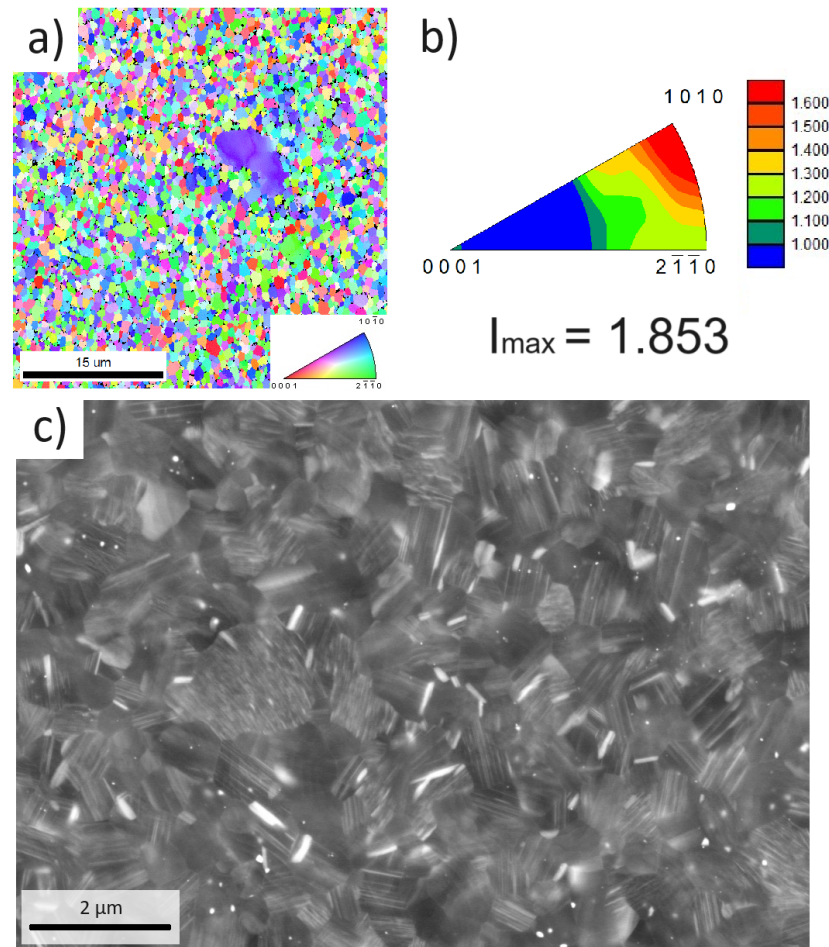
Figure 4.1 Initial microstructure of the investigated MgZnGd alloy: (a) orientation map, (b) IPF texture map with a scale carried out as the multiples of a random density, (c) BSE image. ED is perpendicular to the image plane.

On the BSE image (Figure 4.1 (c)), bright contrast represents regions enriched with Zn and Gd, indicating the formation of solute-enriched SFs, CALs, CANaPs, and precipitates, as it is more visible from the detailed TEM images in Figure 4.2 (a) and (b). Most grains contain individual solute-enriched SFs, CALs, and CANaPs. The SFs and CALs are scattered within the grain's interior and tend to

be relatively short (do not cross entire grains). Moreover, the TEM EDX analysis of two areas of interest in the initial sample (Figure 4.3) confirms that the alloying elements are segregated in the form of precipitates, SFs, CALs, and CANaPs. The dispersion of SFs was calculated from dark field TEM images (e.g., Figure 4.2) for several grains as the number of solute-enriched SFs per unit length (nm). In the initial state, the dispersion of SFs varies significantly between grains. Among the selected grains, the dispersion extended from 0.01 to 0.17 SFs per nm.
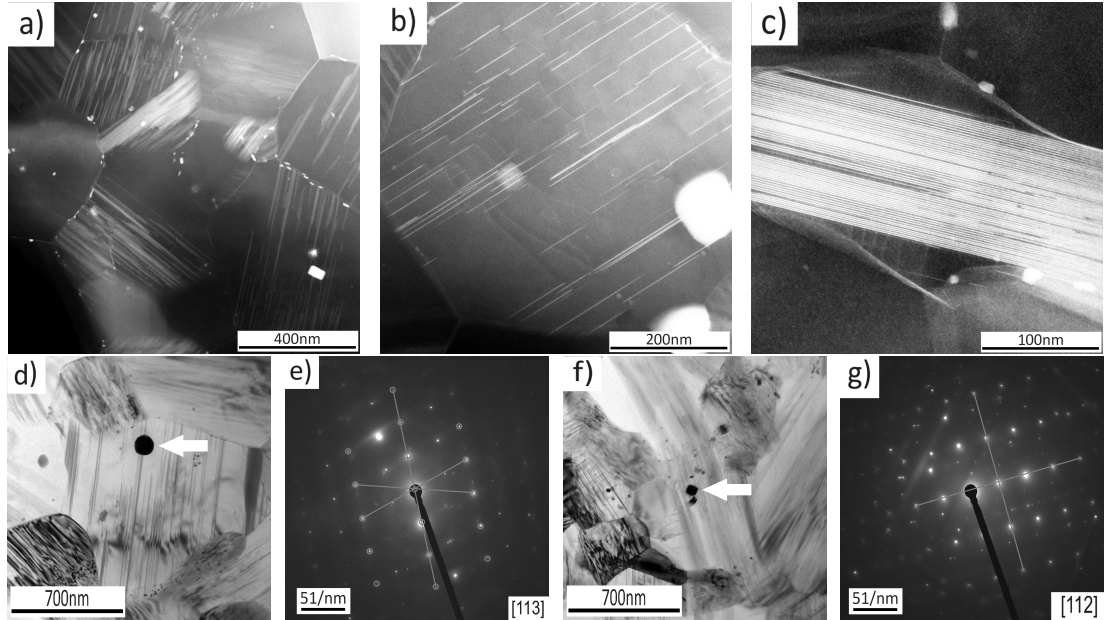
Figure 4.2 The TEM images of the MgZnGd alloy in the initial state in (a-c) DF and (d,f) BF mode indicating (a-b) solute-enriched SFs, (c) CANaPs, (d-e) precipitates Mg_3Gd and (f-g) GdH_2
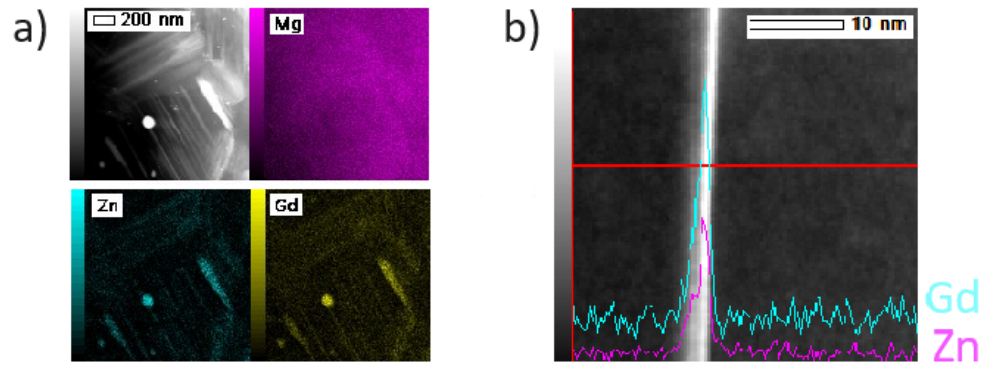
Figure 4.3 The TEM EDX analysis of the MgZnGd alloy in the initial state of (a) LPSO and precipitates containing Zn and Gd, (b) a SF enriched by Zn and Gd

Furthermore, two types of precipitates were found in the alloy, which are shown in Figure 4.2 (d-g). The rectangular-shaped precipitates (Figure 4.2 (f-g)) were identified from their diffraction pattern as GdH_2 with a fcc structure, $Fm\bar{3}m$ symmetry, and a lattice constant $a = 5.3$Å. The precipitate shown in Figure 4.2 (d-e) was identified as Mg_3Gd with a fcc structure, $Fm\bar{3}m$ symmetry, and a lattice constant $a = 7.3$Å.

4.2 Evolution of the microstructure with respect to annealing temperature

The microstructure evolution revealed by the EBSD technique with respect to annealing temperature is shown in Figures 4.4-4.7. The orientation maps and textures are presented in Figure 4.4, while the distribution and average values of grain sizes evaluated from orientation maps are presented in Figure 4.5 and 4.6, respectively. It is obvious, that no significant change is observed between the initial sample and the samples annealed for 2h at 300 °C and 350 °C. Recrystallisation of the microstructure and grain growth starts between 350 °C and 400 °C. From 400 °C, a significant growth of the grain, which attains ~ 3.67 μm after annealing at 500 °C, is observed.

The texture intensity slightly decreases with increasing heat treatment temperature without any distinct trend in intensity peak formation. The overall texture persists to be weak with applied annealing.
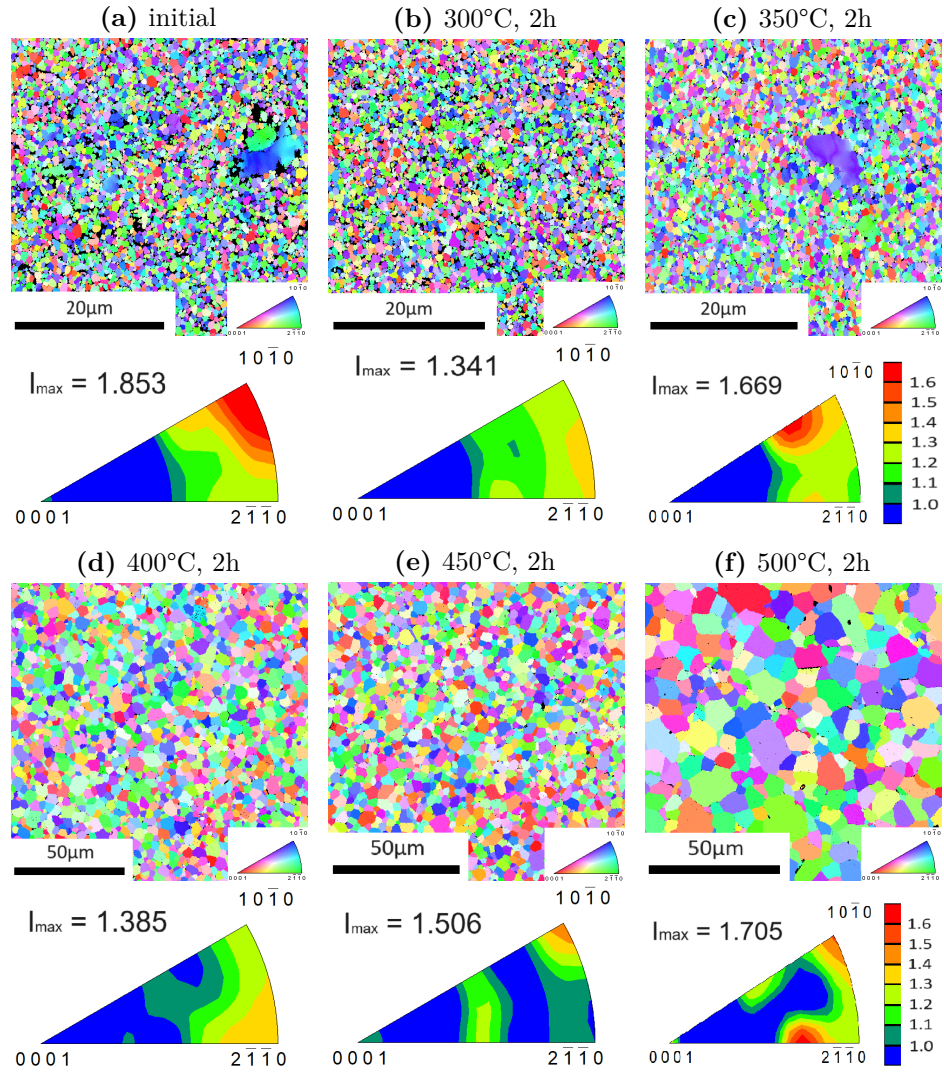
Figure 4.4 The orientation maps and texture plots for the MgZnGd alloy with respect to annealing conditions. ED is perpendicular to the image plane.
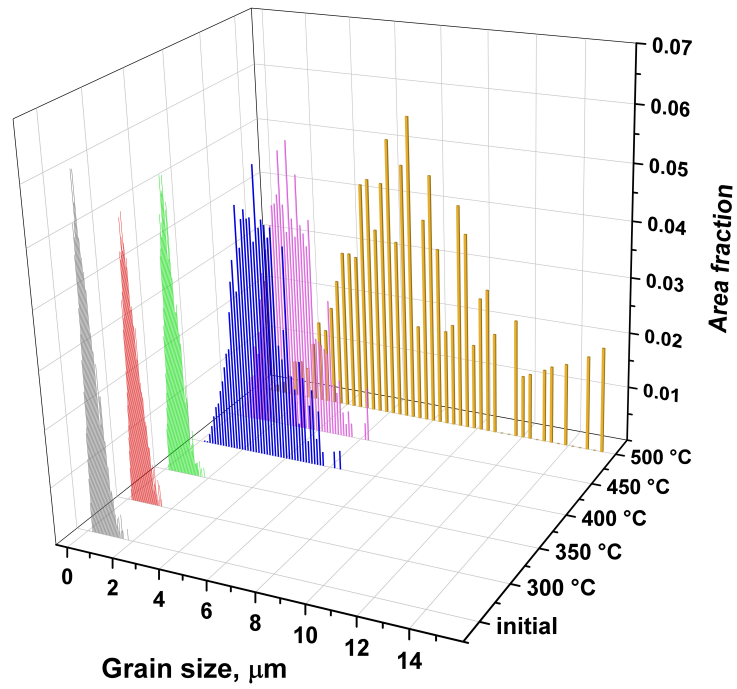
Figure 4.5 The grain size distribution in the MgZnGd alloy concerning annealing temperature
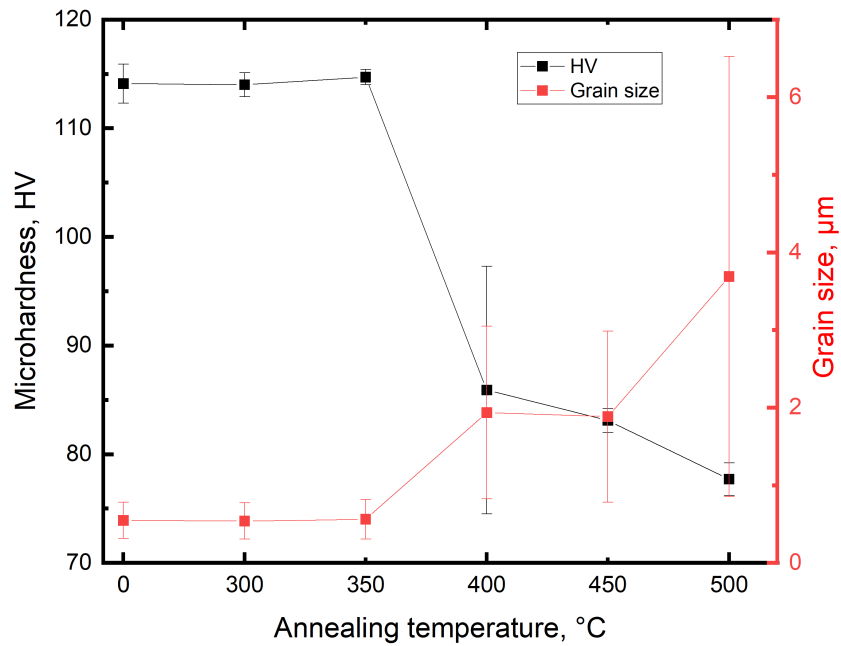
Figure 4.6 The average grain size distribution correlated to the microhardness values of the MgZnGd alloy with respect to annealing temperature

17

The kernel misorientation (KAM) maps in Figure 4.7 represent the local grain misorientation and provide information about internal strain distribution. It is obvious that up to 350 °C, the KAM maps evolve only a little, and present moderate values, which indicates higher dislocation density. Starting from 400 °C, the KAM values overall decrease indicating the formation of strain-free grains.

(a) initial

(b) 300 °C, 2h

(c) 350 °C, 2h

(d) 400 °C, 2h

(e) 450 °C, 2h

(f) 500 °C, 2h
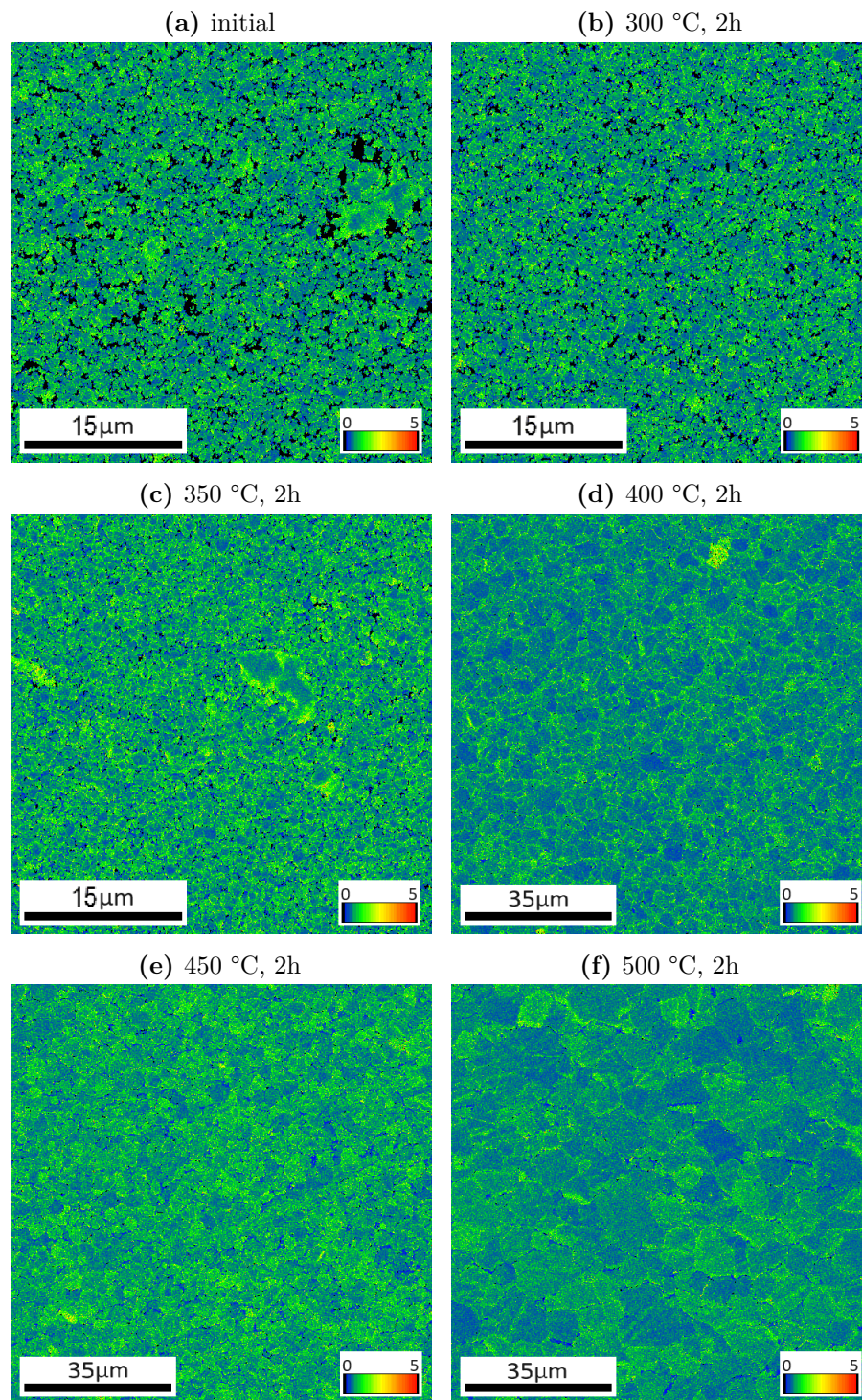
Figure 4.7 The KAM maps of the MgZnGd alloy for various annealing conditions. ED is perpendicular to the image plane.

The change in the distribution of solute-enriched SFs, CALs, CANaPs can be analysed from SEM/BSE and TEM images (Figure 4.8 and 4.9, respectively). The BSE and TEM observations indicate that up to 350 °C the solute-enriched SFs and CALs tend to be relatively scattered in the grains and often do not cross entire grains continuously. Above this temperature, the solute-enriched SFs and CALs become longer and form more compact arrangements. At 500 °C, the solute-enriched SFs are mostly regrouped into CALs and thicker CANaPs of hundreds of solute-enriched SFs. These arrangements usually do not have a long-range periodicity but can become a mixture of several types of LPSO phases. This is visible in the TEM image in Figure 4.9 (h), where two types of LPSO phases can be distinguished: 18R and 24R. Moreover, the dispersion of solute-enriched SFs, was calculated from dark field TEM images for the initial sample and the samples annealed for 2h at 350 °C, 400 °C, and 500 °C. It was found that the dispersion of solute-enriched SFs on the entire grain length doesn't depend on the annealing conditions. However, the analysis was conducted on a dozen grains only, which is not a statistically significant dataset. Nevertheless, from a qualitative view, in the sample annealed at 500 °C, the CANaPs cover only a thin section of the grain, so even if they are formed by hundreds of solute-enriched SFs, and the dispersion ratio of the large grains is consequently comparable to the other samples, large areas without any obstacles for dislocation motion are present in the grains. Additionally, no significant increase in the size of the Mg_3Gd precipitates was observed.

As a preliminary estimation of the mechanical performance of the investigated alloy with respect to applied heat treatment, microhardness measurements have been performed. The correlation of the results of the microhardness measurements with the evolution of the average grain size is presented in Figure 4.6. Initially, the microhardness value of the MgZnGd alloy is 114 HV and stays at this value up to 350 °C. For the sample annealed at 400 °C, there is a drop in microhardness to 86 HV, which further decreases with rising temperature reaching 78 HV for the annealing at 500 °C. The changes in microhardness values are in good agreement with changes in the average grain size estimated from the orientation maps.

(a) initial

(b) 300 °C, 2h

(c) 350 °C, 2h

(d) 400 °C, 2h


(e) 450 °C, 2h

(f) 500 °C, 2h
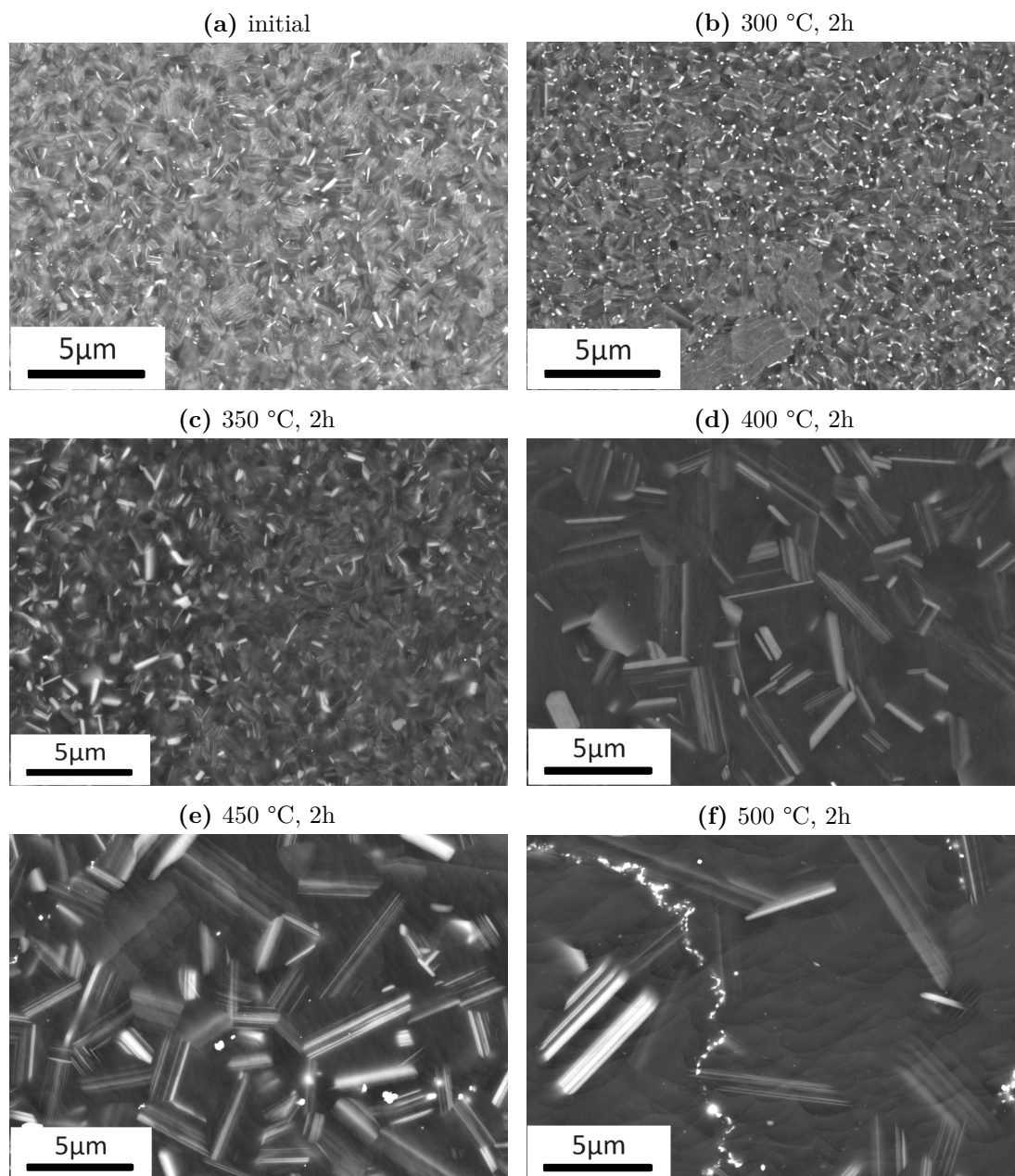
Figure 4.8   The SEM/BSE images of microstructure evolution of the MgZnGd alloy concerning annealing conditions. ED is perpendicular to the image plane.
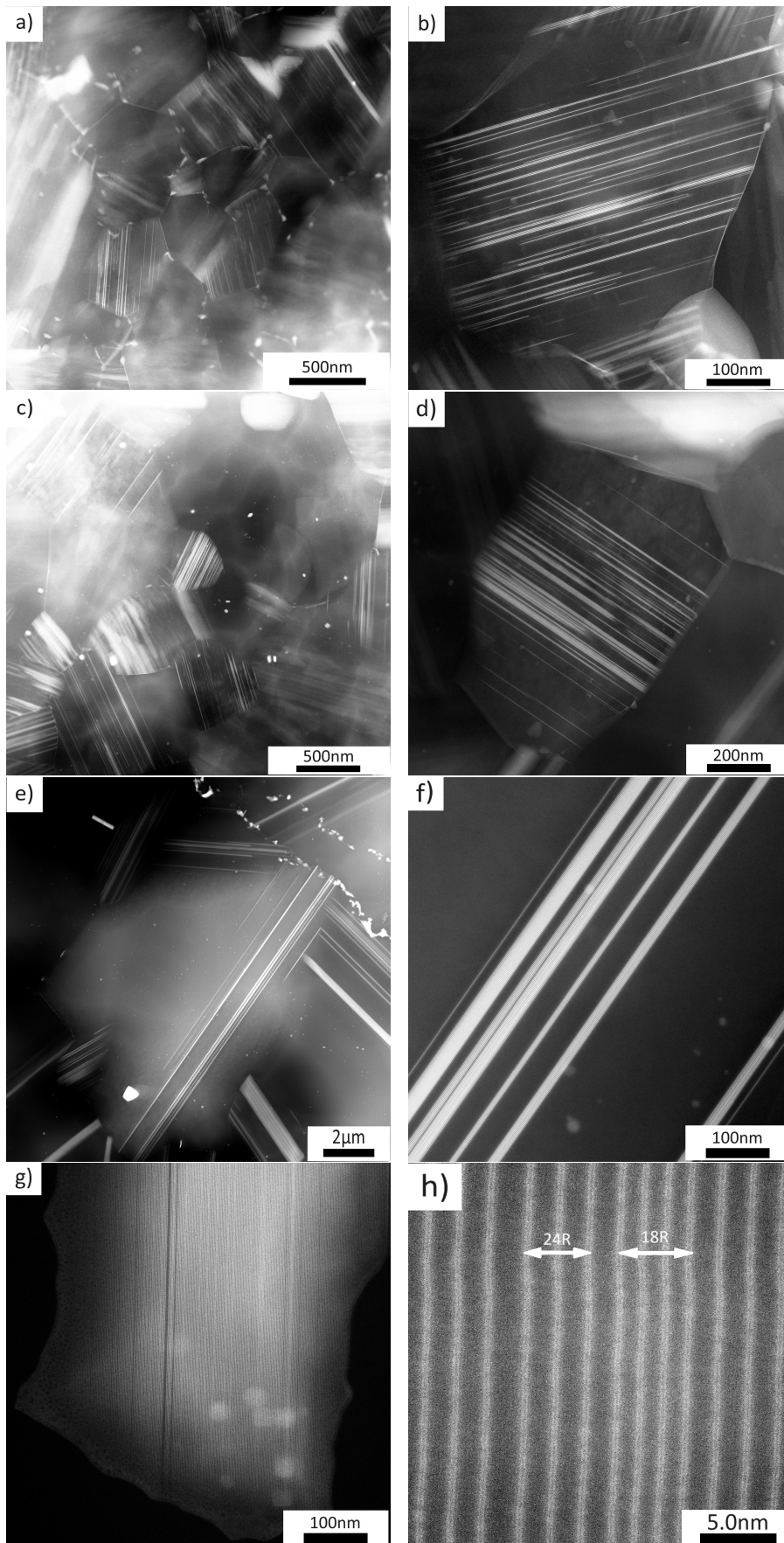
Figure 4.9 The TEM images of the annealed samples of the MgZnGd alloy at (a,b) 350 °C, (c,d) 400 °C, (e,f) 500 °C; and (g,h) an LPSO grain with two types of LPSO phases: 24R and 18R

4.3 Mechanical properties

The compressive and tensile deformation curves of the MgZnGd alloy in the initial state and after annealing for 2h at 350 °C, 400 °C, and 500 °C are shown in Figure 4.10. In the initial and annealed states, the alloy exhibits a reverse tension-compression yield asymmetry, i.e., the values of the compressive yield strength (CYS) are higher than the values of the tensile yield strength (TYS). The YS and elongation values are also summarised in Table 1 together with results of microhardness and the average grain sizes of DRX grains.
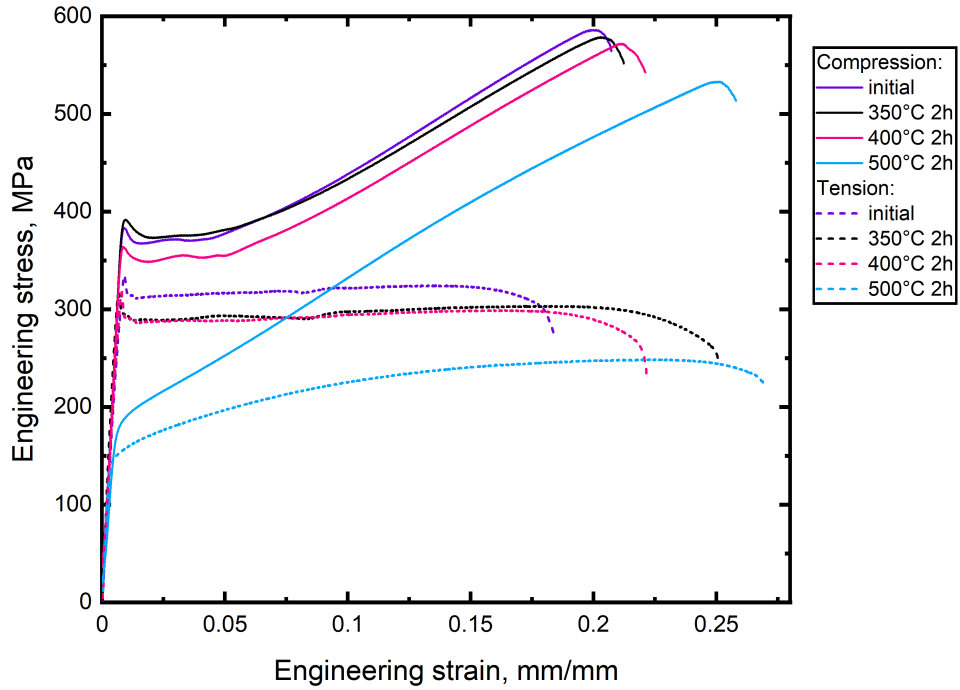
Figure 4.10 Deformation curves of the MgZnGd alloy tested in tension and compression concerning applied heat treatment

Table 4.1 Microstruture characteristics and mechanical properties of the MgZnGd alloys in the initial state and after annealing for 2h at respective temperatures. The elongations were measured with error $\pm$ 1%, ΔYS = CYS - TYS, and $\epsilon_{fC/T}$ is the elongation to fracture in compression/tension

	size of DRX grains μm	HV	CYS MPa	TYS MPa	ΔYS MPa	ϵ_{fC} %	ϵ_{fT} %
initial	0.55 ± 0.23	114 ± 2	372 ± 5	330 ± 5	47	22	18
300 °C	0.54 ± 0.23	114 ± 1	-	-	-	-	-
350 °C	0.56 ± 0.25	115 ± 1	387 ± 5	305 ± 5	82	22	25
400 °C	1.94 ± 1.11	86 ± 2	358 ± 5	307 ± 9	60	23	22
450 °C	1.88 ± 1.10	83 ± 1	-	-	-	-	-
500 °C	3.69 ± 2.84	78 ± 2	178 ± 3	149 ± 1	32	27	27

Annealing at 350 °C results in a minor decrease in strength during tension, while keeping still the same level of strength (within the error range) as that for the initial state in compression. With further increase of annealing temperature up to 400 °C, a decrease in strength in both, tension and compression, compared to the initial state is observed. Annealing at 500 °C for 2h results in a significant decrease of TYS and CYS.

The deformation curves of the sample in the initial state and after annealing up to 400 °C display a similar profile. For these samples, both tensile and compressive deformation curves are characterized by consecutive upper and lower yield points, i.e., the yield point (YP) phenomenon. During compression of the sample in the initial state, after the CYS is reached, the stress suddenly drops by about 17 MPa to a short region of constant stress (plateau), before undergoing strain hardening. The ultimate compression strength reaches almost 200 MPa above the CYS, and fracture occurs shortly after. The sample annealed at 350 °C exhibits similar CYS as the initial state (380 MPa) and after annealing at 400 °C, the CYS value drops down to 360 MPa. During tension of the samples in the initial state, after the TYS is reached, the stress suddenly drops by about 28 MPa, where the material elongates at constant stress, with only slight hardening, followed by fracture at moderate elongation.

After annealing at 500 °C, the strength of the alloy decreases in both compression and tensile loading. Between 400 °C and 500 °C, the CYS drops by approximately 180 MPa and the TYS drops by 150 MPa. Thus, the CYS and TYS values for samples annealed at 500 °C are hardly reaching 180 and 150 MPa, respectively. The yield point phenomenon is no longer present and significant strain hardening occurs above yielding. The ultimate compression yield strength is about 385 MPa higher than CYS, and unlike the other samples, strain hardening takes place in tension as well, with the ultimate tensile strength being 100 MPa higher than TYS. In both compression and tension, the alloy fractures shortly after reaching its ultimate strength.

The elongation to fracture in both tension and compression improves with annealing temperature. The least ductile is the initial sample with an elongation to fracture of $\sim 20\%$. The samples annealed at 350 °C and 400 °C show elongation values between 22% and 25%. The most ductile is the sample annealed at 500 °C with more than 26% elongation before fracture.

Thus, it is obvious that the investigated MgZnGd alloy retains high strength up to 350 °C, and with the following increase in the annealing temperature, the performance of alloys starts to decrease.

5 Discussion

In the initial state, the investigated alloy presents a bimodal microstructure with a weak basal texture resulting from the RSRC processing. The DRX grains are characterized by random orientation, while the non-DRX grains contribute considerably to the slightly higher intensity peak at $\langle 10\bar{1}0 \rangle$ pole, as their $\langle 10\bar{1}0 \rangle$ planes are oriented preferentially perpendicular to ED. This alignment originates from lattice rotations caused by the activation of non-basal slip systems with the $\langle 11\bar{2}0 \rangle$ slip direction during extrusion as reported in [49]. Thus, in the case of the RSRC processing route, the observed intensity increase at the $\langle 10\bar{1}0 \rangle$ pole is formed during the ribbons consolidation step realised by hot extrusion. The presence of the non-DRX grains leading to such pronounced texture was previously reported for commonly used wrought Mg alloys [49] as well as for Mg/LPSO [34, 50] and RSRC Mg-LPSO alloys [40, 39]. As a result of annealing above 350 °C, recovery and recrystallisation begin, which is visible from the KAM maps in Figure 4.7, indicating the reduction of the dislocation density and internal strain in the grains. Recrystalisation also leads to a minor overall texture intensity decrease, (including a decrease of the intensity around the $\langle 10\bar{1}0 \rangle$ pole). This can be explained by the growth of the DRX grains at the expense of the non-DRX grains with their preferential orientation.

From Figures 4.2 and 4.9, it is clear that annealing affects the distribution of solute-enriched SFs and CALs. Since they are obstacles to dislocation motion, their arrangement significantly influences the mechanical properties of the material. In the initial state and for annealing up to 350 °C, most grains contain dispersed solute-enriched SFs and CALs, which can be seen as a cascade of small barricades through the entire grain. Consequently, the dislocations move slowly across a grain, being pinned at each solute-enriched SF, CAL, or CANaP. With annealing above 350 °C, the SFs and CALs regroup and form thicker and longer CANaPs, which are more effective at blocking dislocations. However, dislocations might have longer mean free path for their moving in the grains of the alloy annealed at 500 °C before being pinned on a CANaP, since the CANaPs are usually concentrated in a small section of the already large grain.

Besides solute-enriched SFs, CALs, and CANaPs, two types of precipitates, Mg_3Gd and GdH_2 were identified as seen in Figure 4.2 (d-g). The formation of RE hydrides is commonly observed in Mg-RE alloys, however, their origin still remains unclear [51, 52, 53]. Furthermore, small LPSO grains containing a mixture of a few LPSO types have been identified, Figure 4.2 (c) and Figure 4.7 (g,h).

From microstructure analysis, it is obvious that grain size of the investigated alloy does not change much up to 350 °C, where the average grain size is still about 560 nm. Above 400 °C, a significant grain growth is observed. Hence, the developed microstructure comprises features that ensure thermal stability up to 350 °C.

The observed complex microstructure of MgZnGd alloy is comparable to those of other low-alloyed RSRC Mg-TM-RE alloys [39]. It was reported that using a low amount of alloying elements (less than 2 at. % of Y or Gd) in Mg-Zn-based alloys together with the RSRC processing technique leads to the formation of solute-enriched SFs and CALs dispersed in the fine DRX and large non-DRX

grains. Such microstructure results in enhanced mechanical properties and shows promising corrosion resistance [54], which increases the potential of developed materials in their practical use. Moreover, the MgZnY alloy was also characterised by high thermal stability of the microstructure [40]. It was reported by Tang et al. [55], that alloying with Gd and Y can increase the thermal stability of a MgZnYZr alloy, because Gd and Y can effectively change the stacking fault energy and contribute to the formation of nanocrystals/precipitates at grain boundaries.

The microhardness of the MgZnGd alloy in the initial state was 114 HV, which within the error is comparable to the microhardness value observed in the RSRC Mg-0.56Zn-1.5Y (at.%) alloy [40]. The elevated hardness in both alloys can be attributed to the small grain size through the Hall-Petch relation [20, 21], and the presence of solute-enriched SFs, CALs, CANaPs, and precipitates. The microhardness measurements indicate that hardness also correlates with grain size (see Figure 4.6). It is obvious that the microhardness as well as the corresponding average grain size remain almost constant up to 350 °C. Above this temperature, recrystallisation, grain growth, and the redistribution of SFs cause the microhardness to drop owing to lower dislocation densities and fewer grain boundaries.

Regarding mechanical properties, the alloy in the initial state has high yield strength and moderate elongation. The results are comparable with the low-allowed Mg-Zn-Y and Mg-Zn-Gd alloy processed by the RSRC technique reported in [39]. As it was explained by Yamasaki et al. [7], the enhanced properties can be achieved in extruded Mg-LPSO alloys by the bimodal character of the microstructure, where the non-DRX grains and LPSO phase contributes to the strengthening of the alloy, whereas the DRX grains randomly oriented improve its ductility. Moreover, in the case of the RSRC alloys, the material is strengthened by the presence of solute-enriched SFs, CALs, CANaPs, precipitates, and the small LPSO grains [5].

Overall, the deformation curves in compression exhibit the same tendency with heat treatment as the microhardness. The behavior in compression remains unchanged up to 350 °C. In tension, the sample annealed at 350 °C already shows lower TYS than that for the initial state and the same tensile strength as the sample annealed at 400 °C, which can be attributed to differences in the activation and efficiency of slip systems between compression and tension. Nonetheless, the profile of both the compression and tensile curves do not change significantly with heat treatment up to 400 °C. Above 350 °C, recrystallisation and grain growth take place leading to increase in the number of DRX α-Mg grains. This leads to an increase in elongation and a slight decrease in strength. The loading curves also present a reverse tension-compression asymmetry, i.e., the compression curves are higher than the tensile curves. According to Garces et al. [29], the onset of plasticity is controlled by the volume fraction of DRX grains. When the volume fraction is low, yield is controlled by the dislocation slip on the $\langle 11\bar{2}0 \rangle \{00\bar{0}2\}$ slip system, which may be easier to activate in tension than in compression. The asymmetry ΔYS is however relatively consistent despite annealing. Moreover, Drozdenko et al. reported [39] that for Mg-Zn-based alloys the alloying with Gd results in lower asymmetry in the initial state compared to alloying with Y or Nd.

Heat treatment above 400 °C leads to further decline in the the yield strength due to recrystallisation, grain growth, and the redistribution of SFs. The yield

strength of the sample annealed at 500 °C is less than half that of the initial state and the profile of the loading curves differs significantly.

For the samples in the initial state and after heat treatment up to 400 °C, the yield point phenomenon is observed for both compression and tensile loading. In the case of compression loading of the samples annealed up to 400 °C, the lower YP. The YP phenomenon has been previously observed by Barnett et al. for the AZ31 Mg alloy and attributed to twinning activity [56]. However, addressed AZ31 had a significantly greater grain size than the present RSRC MgZnGd alloy. The YP phenomenon has also been observed by Minarik et al. in the WE43 Mg alloy [57], which had finer grains than MgZnGd. The sharp yield point in that case was associated with significant grain refinement and precipitation. However, the ultra fine-grained microstructure of the investigated RSRC MgZnGd alloy is also characterized by solute-enriched SFs, CALs and CANaPs, which play a role as obstacles for twinning activity. Thus, deformation in compression is supposed to be solely dislocation-mediated.

In the case of tensile loading, as explained in Drozdenko et al. [58], the YP phenomenon occurs due to the pinning of dislocations on solute atoms and SFs, and after reaching a certain external load, these non-basal pinned dislocations are suddenly released causing the stress drop from upper YP to lower YP. Furthermore, the SFs and the high density of grain boundaries limit the propagation of the deformation along the sample, and rather localised deformation is observed. During the deformation of the samples after heat treatment at 500 °C the YP phenomenon is no longer observed, which could be explained by the significant decrease of the number of dislocations together with the rearrangement of the SFs and CALs.

The tensile curves of the samples annealed up to 400 °C indicate a balance between hardening (pinning of dislocations on precipitates) and softening (release of the pinned dislocations). For the sample annealed at 500 °C, hardening dominates over softening, which is indicated by the rising profile of the loading curve. Plastic deformation in tension is accommodated by dislocation slip only, no twinning has been reported for tension loading in either wrought Mg-Gd alloys with coarse grains [59] or the RSRC MgZnY alloys with fine grains [58].

Conclusions

The application of the RSRC technique to the low-alloyed Mg-0.56Zn-1.5Gd (at.%) results in formation of a bimodal microstructure with fine DRX grains and larger non-DRX grains, both containing individually distributed solute-enriched SFs and CALs. These microstructure features together with weak texture lead to overall enhanced mechanical properties reflected in high yield strength (330 and 370 MPa in tension and compression, respectively) and moderate elongation (above 20 %).

The obtained results revealed that annealing for 2 h at temperatures up to 350 °C does not lead to a significant change in the microstructure, with an average grain size of about 560 nm. The stability of the microstructure is supported by microhardness measurements and deformation tests, where values are comparable to those observed in the initial state.

The heat treatment at 400 and 450 °C leads to a significant grain size increase together with a reduction in the internal strain and the regrouping of individually distributed solute-enriched SFs into CALs and thicker CANaPs. These microstructure changes lead to a slight decrease in the hardness and mechanical properties. Regarding ductility, the alloy has already moderate elongation in the initial state, which improves with annealing. Nevertheless, the shape of deformation curves remains the same with applied annealing up to 400 °C indicating preservation of active deformation mechanisms.

With further increase in annealing temperature up to 500 °C, a massive grain growth (up to 3.7 µm) and regrouping of the solute-enriched SFs into CALs and thicker CANaPs are observed. These microstructure changes lead to an increase in the free mean path of moving dislocations. Thus, the yield strength of the alloy decreases significantly, hardly reaching 180 and 150 MPa in compression and tension, respectively.

Future perspectives

The findings indicate that the alloy possesses good thermal stability, making it highly suitable for a wide range of applications requiring thermal resistance. For further understanding and improvement of low-alloyed Mg alloys, several questions can be addressed in future research. For instance, the mechanisms underlying the mechanical properties of the MgZnGd alloy or the relation between the microstructural features and corrosion behavior require further investigation.

References

1. INTERNATIONAL MAGNESIUM ASSOCIATION. *Magnesium applications* [online]. [visited on 2024-07-17]. Available from: `https://www.intlmag.org/page/app_medical_ima`.

2. CHEN, Y.; XU, Z.; SMITH, C.; SANKAR, J. Recent advances on the development of magnesium alloys for biodegradable implants. *Acta Biomaterialia*. 2014, vol. 10, no. 11, pp. 4561–4573. Available from DOI: `10.1016/j.actbio.2014.07.005`.

3. PERON, M.; TORGERSEN, J.; BERTO, F. Mg and Its Alloys for Biomedical Applications: Exploring Corrosion and Its Interplay with Mechanical Failure. *Metals*. 2017, vol. 7, no. 7. Available from DOI: `10.3390/met7070252`.

4. INOUE, A.; KAWAMURA, Y.; MATSUSHITA, M.; HAYASHI, K.; KOIKE, J. Novel hexagonal structure and ultrahigh strength of magnesium solid solution in the Mg–Zn–Y system. *Journal of Materials Research*. 2001, vol. 16, no. 7, pp. 1894–1900. Available from DOI: `10.1557/JMR.2001.0260`.

5. KAWAMURA, Y.; HAYASHI, K.; INOUE, A.; MASUMOTO, T. Rapidly solidified powder metallurgy $Mg_{97}Zn_1Y_2$ alloys with excellent tensile yield strength above 600 MPa. *Materials Transactions*. 2001, vol. 42, no. 7, pp. 1172–1176. Available from DOI: `10.2320/matertrans.42.1172`.

6. KAWAMURA, Y.; KASAHARA, T.; IZUMI, S.; YAMASAKI, M. Elevated temperature Mg97Y2Cu1 alloy with long period ordered structure. *Scripta Materialia*. 2006, vol. 55, no. 5, pp. 453–456. Available from DOI: `10.1016/j.scriptamat.2006.05.011`.

7. YAMASAKI, M.; HASHIMOTO, K.; HAGIHARA, K.; KAWAMURA, Y. Effect of multimodal microstructure evolution on mechanical properties of Mg–Zn–Y extruded alloy. *Acta Materialia*. 2011, vol. 59, no. 9, pp. 3646–3658. Available from DOI: `/10.1016/j.actamat.2011.02.038`.

8. YAMASAKI, M.; HAYASHI, N.; IZUMI, S.; KAWAMURA, Y. Corrosion behavior of rapidly solidified Mg–Zn–rare earth element alloys in NaCl solution. *Corrosion Science*. 2007, vol. 49, no. 1, pp. 255–262. Available from DOI: `10.1016/j.corsci.2006.05.017`.

9. DROZDENKO, D.; YAMASAKI, M.; MÁTHIS, K.; DOBROŇ, P.; LUKÁČ, P.; KIZU, N.; INOUE, S.; KAWAMURA, Y. Optimization of mechanical properties of dilute Mg-Zn-Y alloys prepared by rapid solidification. *Materials and Design*. 2019, vol. 181, p. 107984. Available from DOI: `10.1016/j.matdes.2019.107984`.

10. CALLISTER, W.D.; RETHWISCH, D.G. *Materials Science and Engineering: An Introduction*. Wiley, 2008. Wiley Plus Products. ISBN 9780470448649.

11. SCHMID, E.; WASSERMANN, G. Über die Textur gezogener Magnesium- und Zinkdrähte. *Naturwissenschaften*. 1929, vol. 17, pp. 312–314.

12. BARBER, B.; BEST, C. *Slip geometry: the critical resolved shear stress* [online]. [visited on 2024-07-17]. Available from: `https://www.doitpoms.ac.uk/tlplib/slip/slip_geometry.php`.

13. YOO, M.H. Slip, twinning, and fracture in hexagonal close-packed metals. *Metallurgical Transactions A*. 1981, vol. 12, pp. 409–418. Available from DOI: `10.1007/BF02648537`.

14. AVEDESIAN, M.M.; BAKER, H.; COMMITTEE, A.S.M.I.H. *ASM Specialty Handbook: Magnesium and Magnesium Alloys*. ASM International, 1999. ASM Specialty Handbook. ISBN 978-0-87170-657-7.

15. MISES, R. V. Mechanik der plastischen Formänderung von Kristallen. *Zeitschritf für Angewandte Mathematik und Mechanik*. 1928, vol. 8, no. 3, pp. 161–185. Available from DOI: `10.1002/zamm.19280080302`.

16. BARNETT, M.R. Twinning and the ductility of magnesium alloys: Part I: "Tension" twins. *Materials Science and Engineering A*. 2007, vol. 464, no. 1, pp. 1–7. Available from DOI: `10.1016/j.msea.2006.12.037`.

17. BARNETT, M.R. Twinning and the ductility of magnesium alloys: Part II. "Contraction" twins. *Materials Science and Engineering A*. 2007, vol. 464, no. 1, pp. 8–16. Available from DOI: `10.1016/j.msea.2007.02.109`.

18. ZHOU, R.; ROY, A.; SILBERSCHMIDT, V.V. A crystal-plasticity model of extruded AM30 magnesium alloy. *Computational Materials Science*. 2019, vol. 170, p. 109140. Available from DOI: `10.1016/j.commatsci.2019.109140`.

19. KAINER, K.U.; MORDIKE, B.L. *Magnesium alloys and their applications*. Vol. 1174. Wiley-Vch Weinheim, Germany, 2000.

20. HALL, E. O. The Deformation and Ageing of Mild Steel: III Discussion of Results. *Proceedings of the Physical Society. Section B*. 1951, vol. 64, no. 9, p. 747. Available from DOI: `10.1088/0370-1301/64/9/303`.

21. PETCH, N. J. The Cleavage Strength of Polycrystals. *Journal of the Iron and Steel Institute*. 1953, vol. 174, pp. 25–28.

22. YIN, D.L.; WANG, J.T.; LIU, J.Q.; ZHAO, X. On tension–compression yield asymmetry in an extruded Mg–3Al–1Zn alloy. *Journal of Alloys and Compounds*. 2009, vol. 478, no. 1, pp. 789–795. Available from DOI: `10.1016/j.jallcom.2008.12.033`.

23. YIN, D.D.; BOEHLERT, C.J.; LONG, L.J.; HUANG, G.H.; ZHOU, H.; ZHENG, J.; WANG, Q.D. Tension-compression asymmetry and the underlying slip/ twinning activity in extruded Mg–Y sheets. *International Journal of Plasticity*. 2021, vol. 136, p. 102878. Available from DOI: `10.1016/j.ijplas.2020.102878`.

24. BOHLEN, J.; YI, S.; LETZIG, D.; KAINER, K. Effect of rare earth elements on the microstructure and texture development in magnesium–manganese alloys during extrusion. *Materials Science and Engineering A*. 2010, vol. 527, pp. 7092–7098. Available from DOI: `10.1016/j.msea.2010.07.081`.

25. ABE, E.; ONO, A.; ITOI, T.; YAMASAKI, M.; KAWAMURA, Y. Polytypes of long-period stacking structures synchronized with chemical order in a dilute Mg–Zn–Y alloy. *Philosophical Magazine Letters*. 2011, vol. 91, no. 10, pp. 690–696. Available from DOI: `10.1080/09500839.2011.609149`.

26. KAWAMURA, Y.; YAMASAKI, M. Formation and Mechanical Properties of $Mg_{97}Zn_1RE_2$ Alloys with Long-Period Stacking Ordered Structure. *Materials transactions*. 2007, vol. 48, no. 11, pp. 2986–2992. Available from DOI: `10.2320/matertrans.MER2007142`.

27. HAGIHARA, K.; UEYAMA, R.; YAMASAKI, M.; KAWAMURA, Y.; NAKANO, T. Surprising increase in yield stress of Mg single crystal using long-period stacking ordered nanoplates. *Acta Materialia*. 2021, vol. 209, p. 116797. Available from DOI: `10.1016/j.actamat.2021.116797`.

28. JAIN, J.; POOLE, W.J.; SINCLAIR, C.W.; GHARGHOURI, M.A. Reducing the tension–compression yield asymmetry in a Mg–8Al–0.5Zn alloy via precipitation. *Scripta Materialia*. 2010, vol. 62, no. 5, pp. 301–304. Available from DOI: `10.1016/j.scriptamat.2009.11.024`.

29. GARCES, G.; PEREZ, P.; CABEZA, S.; LIN, H.K.; KIM, S.; GAN, W.; ADEVA, P. Reverse tension/compression asymmetry of a Mg–Y–Zn alloys containing LPSO phases. *Materials Science and Engineering: A*. 2015, vol. 647, pp. 287–293. Available from DOI: `10.1016/j.msea.2015.09.003`.

30. MATSUDA, M.; II, S.; KAWAMURA, Y.; IKUHARA, Y.; NISHIDA, M. Interaction between long period stacking order phase and deformation twin in rapidly solidified Mg97Zn1Y2 alloy. *Materials Science and Engineering: A*. 2004, vol. 386, no. 1, pp. 447–452. Available from DOI: `10.1016/j.msea.2004.08.006`.

31. GARCES, G.; MUÑOZ-MORRIS, M.A.; MORRIS, D.G.; JIMENEZ, J.A.; PEREZ, P.; ADEVA, P. The role of extrusion texture on strength and its anisotropy in a Mg-base alloy composed of the Long-Period-Structural-Order phase. *Intermetallics*. 2014, vol. 55, pp. 167–176. Available from DOI: `10.1016/j.intermet.2014.07.015`.

32. HAGIHARA, K.; YAMASAKI, M.; HONNAMI, M.; IZUNO, H.; TANE, M.; NAKANO, T.; KAWAMURA, Y. Crystallographic nature of deformation bands shown in Zn and Mg-based long-period stacking ordered (LPSO) phase. *Philosophical Magazine*. 2015, vol. 95, no. 2, pp. 132–157. Available from DOI: `10.1080/14786435.2014.987843`.

33. GARCÉS, G.; MÁTHIS, K.; MEDINA, J.; HORVÁTH, K.; DROZDENKO, D.; OÑORBE, E.; DOBROŇ, P.; PÉREZ, P.; KLAUS, M.; ADEVA, P. Combination of in-situ diffraction experiments and acoustic emission testing to understand the compression behavior of Mg-Y-Zn alloys containing LPSO phase under different loading conditions. *International Journal of Plasticity*. 2018, vol. 106, pp. 107–128. Available from DOI: `10.1016/j.ijplas.2018.03.004`.

34. HAGIHARA, K.; KINOSHITA, A.; SUGINO, Y.; YAMASAKI, M.; KAWAMURA, Y.; YASUDA, H.Y.; UMAKOSHI, Y. Effect of long-period stacking ordered phase on mechanical properties of Mg97Zn1Y2 extruded alloy. *Acta Materialia*. 2010, vol. 58, no. 19, pp. 6282–6293. Available from DOI: `10.1016/j.actamat.2010.07.050`.

35. Horváth, K.; Drozdenko, D.; Daniš, S.; Garcés, G.; Máthis, K.; Kim, S.; Dobroň, P. Characterization of Microstructure and Mechanical Properties of Mg–Y–Zn Alloys with Respect to Different Content of LPSO Phase. *Advanced Engineering Materials*. 2018, vol. 20, no. 1, p. 1700396. Available from DOI: `10.1002/adem.201700396`.

36. Horváth, K.; Drozdenko, D.; Garcés, G.; Dobroň, P.; Máthis, K. Characterization of the Acoustic Emission Response and Mechanical Properties of Mg Alloy with LPSO Phase. *Materials Science Forum*. 2017, vol. 879, pp. 762–766. Available from DOI: `10.4028/www.scientific.net/MSF.879.762`.

37. Hagihara, K.; Yokotani, N.; Umakoshi, Y. Plastic deformation behavior of Mg12YZn with 18R long-period stacking ordered structure. *Intermetallics*. 2010, vol. 18, no. 2, pp. 267–276. Available from DOI: `10.1016/j.intermet.2009.07.014`.

38. Oñorbe, E.; Garces, G.; Pérez, P.; Adeva, P. Effect of the LPSO volume fraction on the microstructure and mechanical properties of Mg-Y2X-Zn X alloys. *Journal of Materials Science*. 2012, vol. 47, pp. 1085–1093. Available from DOI: `10.1007/s10853-011-5899-4`.

39. Drozdenko, D.; Fekete, K.; Dobroň, P.; Németh, G.; Veselý, J.; Nishimoto, S.; Yamasaki, M.; Kawamura, Y. The microstructure and anisotropic deformation behavior of rapidly solidified ribbon consolidated Mg-Zn-X (X = Y, Gd, Nd) alloys. *Journal of Alloys and Compounds*. 2023, vol. 944, p. 169175. Available from DOI: `10.1016/j.jallcom.2023.169175`.

40. Fekete, K.; Drozdenko, D.; Cejpek, P.; Dobroň, P.; Veselý, J.; Yamasaki, M.; Kawamura, Y. Thermal stability of the microstructure of rapidly solidified ribbon-consolidated Mg97.94Zn0.56Y1.5 alloy. *Materials Characterization*. 2021, vol. 183, p. 111618. Available from DOI: `10.1016/j.matchar.2021.111618`.

41. Kawamura, Y.; Yamagata, H.; Inoue, S.; Kiguchi, T.; Chattopadhyay, K. Kink bands and strengthening of millefeuille-structured magnesium alloys by cluster-arranged nanoplates (CANaPs): The case of Mg-0.4Zn-1.0Y alloy. *Journal of Alloys and Compounds*. 2023, vol. 939, p. 168607. ISSN 0925-8388. Available from DOI: `10.1016/j.jallcom.2022.168607`.

42. Dunlap, M.; Adaskaveg, J.E. *Introduction to the scanning electron microscopy*. Facility for advanced instrumentation, 1997.

43. Nanoscience Instruments. *Scanning electron microscopy* [online]. [visited on 2024-07-17]. Available from: `https://www.nanoscience.com/techniques/scanning-electron-microscopy/`.

44. JEOL. *Electron backscatter diffraction* [online]. [visited on 2024-07-17]. Available from: `https://www.jeol.com/words/semterms/20121024.032159.php#gsc.tab=0`.

45. Nanoscience Instruments. *Transmission electron microscopy* [online]. [visited on 2024-07-17]. Available from: `https://www.nanoscience.com/techniques/transmission-electron-microscopy/`.

46. BHATTACHARYYA, S.; KOCH, C.; RÜHLE, M. Projected Potential Profiles across Intergranular Glassy Films. *Journal of The Ceramic Society of Japan.* 2006, vol. 114, pp. 1005–1012. Available from DOI: `10.2109/jcersj.114.1005`.

47. MAGNESIUM RESEARCH CENTER KUMAMOTO UNIVERSITY. *Research and Faculty* [online]. [visited on 2024-07-17]. Available from: `https://www.mrc.kumamoto-u.ac.jp/en/research/`.

48. MATHERS, G. *Hardness testing part 1* [online]. [visited on 2024-07-17]. Available from: `https://www.twi-global.com/technical-knowledge/job-knowledge/hardness-testing-part-1-074`.

49. MAYAMA, T.; NODA, M.; CHIBA, R.; KURODA, M. Crystal plasticity analysis of texture development in magnesium alloy during extrusion. *International Journal of Plasticity.* 2011, vol. 27, no. 12, pp. 1916–1935. Available from DOI: `10.1016/j.ijplas.2011.02.007`.

50. JONO, Y.; YAMASAKI, M.; KAWAMURA, Y. Effect of LPSO Phase-Stimulated Texture Evolution on Creep Resistance of Extruded Mg-Zn-Gd Alloys. *Materials transactions.* 2013, vol. 54, pp. 703–712. Available from DOI: `10.2320/matertrans.MI201218`.

51. ZHU, S.M.; NIE, J.F.; GIBSON, M.A.; EASTON, M.A. On the unexpected formation of rare earth hydrides in magnesium–rare earth casting alloys. *Scripta Materialia.* 2014, vol. 77, pp. 21–24. Available from DOI: `10.1016/j.scriptamat.2014.01.007`.

52. YANG, Y.; PENG, L.; FU, P.; HU, B.; DING, W. Identification of NdH2 particles in solution-treated Mg–2.5%Nd (wt.%) alloy. *Journal of Alloys and Compounds.* 2009, vol. 485, no. 1, pp. 245–248. Available from DOI: `10.1016/j.jallcom.2009.06.040`.

53. PENG, Z.Z.; SHAO, X.H.; JIN, Q.Q.; LI, C.H.; MA, X.L. Deformation induced precipitation of nano-particles in an Mg88Co5Y7 alloy. *Scripta Materialia.* 2016, vol. 116, pp. 57–61. Available from DOI: `10.1016/j.scriptamat.2016.01.031`.

54. DROZDENKO, D.; YAMASAKI, M.; MÁTHIS, K.; DOBROŇ, P.; INOUE, S.; KAWAMURA, Y. Revealing the Microstructural Aspects of the Corrosion Dynamics in Rapidly Solidified Mg-Zn-Y Alloys Using the Acoustic Emission Technique. *Materials.* 2021, vol. 14, no. 24. Available from DOI: `10.3390/ma14247828`.

55. TANG, L.; ZHAO, Y.; ISLAMGALIEV, R.K.; VALIEV, R.Z.; ZHU, Y.T. Microstructure and thermal stability of nanocrystalline Mg-Gd-Y-Zr alloy processed by high pressure torsion. *Journal of Alloys and Compounds.* 2017, vol. 721, pp. 577–585. Available from DOI: `10.1016/j.jallcom.2017.05.164`.

56. BARNETT, M.R.; NAVE, M.D.; GHADERI, A. Yield point elongation due to twinning in a magnesium alloy. *Acta Materialia.* 2012, vol. 60, no. 4, pp. 1433–1443. Available from DOI: `10.1016/j.actamat.2011.11.022`.

57. Minárik, P.; Veselý, J; Král, R.; Bohlen, J.; Kubásek, J.; Janeček, M.; Stráská, J. Exceptional mechanical properties of ultra-fine grain Mg-4Y-3RE alloy processed by ECAP. *Materials Science and Engineering A*. 2017, vol. 708, pp. 193–198. Available from DOI: 10.1016/j.msea.2017.09.106.

58. Drozdenko, D.; Fekete, K.; Dobroň, P.; Knapek, M.; Mathis, K.; Minárik, P.; Yamasaki, M.; Kawamura, Y. The yield point phenomenon in ultrafine-grained dilute Mg-Zn-Y alloys. *Materials Letters*. 2023, vol. 330, p. 133315. Available from DOI: 10.1016/j.matlet.2022.133315.

59. Luo, X.; Feng, Z.; Yu, T.; Luo, J; Huang, T; Wu, G.; Hansen, N.; Huang, X. Transitions in mechanical behavior and in deformation mechanisms enhance the strength and ductility of Mg-3Gd. *Acta Materialia*. 2020, vol. 183, pp. 398–407. Available from DOI: 10.1016/j.actamat.2019.11.034.

List of abbreviations

RSRC	rapidly solidified ribbon consolidation
hcp	hexagonal close-packed
CRSS	critical resolved shear stress
YS	yield strength
TYS	tensile yield strength
CYS	compression yield strength
TM	transition metal
RE	rare earth element
LPSO	long-period stacking order
DRX	dynamic recrystallisation
SF	stacking fault
CAL	cluster arranged layer
CANaP	cluster arranged nanoplate
SEM	scanning electron microscopy
TEM	transmission electron microscopy
BSE	back-scattered electrons
STEM	scanning TEM
BF	bright field
DF	dark field
EDX	energy-dispersive X-ray spectroscopy
ED	extrusion direction
YP	yield point
IPF	inverse pole figure
KAM	kernel average misorientation